1   **The Rhyolite Factory: Insights from rhyolite-MELTS geobarometry of plutonic rocks and**

2   **associated volcanics**

3   Guilherme A. R. Gualda[1], Calvin F. Miller[1], Blake M. Wallrich[1]

4   [1]Earth & Environmental Sciences, Vanderbilt University, Nashville, TN 37235

5

6 **ABSTRACT**

7 Magmatic systems feed eruptions to the surface; lead to the formation of ore deposits; provide energy

8 for geothermal systems; and are key to Earth's differentiation. While it is commonly accepted that silicic

9 magmatic systems span much of the crust, little direct evidence is available for their vertical continuity (or

10 lack thereof), or for the distribution of melt within them.

11 We focus on Miocene plutonic and volcanic units exposed in the Colorado Extensional Corridor, SW USA.

12 Plutonic units (Searchlight Pluton–SLP, Aztec Wash Pluton–AWP, and Spirit Mountain Batholith–SMB)

13 consist primarily of coarse-grained granitoids rich in feldspar that can be credibly considered cumulates.

14 Marginal facies and fine-grained dikes and sills are interpreted to record melt compositions that fed the

15 plutons. Leucogranite dikes and roof units were extracted from the crystallizing plutons. The nearby

16 Upper Highland Range Volcanics record compositions extracted from the SLP system.

17 We use whole-rock compositions of granitoids and rhyolites to calculate extraction pressures, and glass

18 compositions from volcanic rocks to calculate pre-eruptive storage pressures using rhyolite-MELTS. We

19 seek pressures consistent with assemblages containing quartz+2 feldspars±magnetite±ilmenite (Q2F or

20 Q2FMI assemblages). We use the calculated pressures to assess the distribution of magma in silicic

21 magmatic crustal columns.

22 The dataset reveals three main clusters of compositions and pressures: 72-74.5 wt.% SiO_2, 450-370 MPa

23 (Q2F extraction); 75.5-77 wt.% SiO_2, 300-185 MPa (Q2FMI extraction and pre-eruptive storage); 77.5-78

24 wt.% SiO_2, 180-120 MPa (Q2FMI extraction and pre-eruptive storage). Compositions attributed to

25 cumulates (based on texture, major and trace-element compositions) do not typically yield extraction

26 pressures, suggesting that rhyolite-MELTS can generally distinguish magmatic from cumulatic

27 compositions.

28 Our data show that magma distribution spanned from the middle crust to the surface, with well-defined

29 gaps in pressure between the three groups. Magma mushes were located in the middle crust (~400 MPa,

30   ~15 km depth), from which magmas that fed the shallow plutonic units were derived – there is no

31   exposed record of these magma mushes, and they are inferred from extraction pressures for the less

32   evolved fine-grained rocks. We infer two sets of shallower mush bodies that fed eruptions to the surface.

33   The leucogranite roof zones represent bodies of melt-dominated magma that failed to erupt and instead

34   solidified in the subsurface. Magma distribution is vertically discretized, rather than continuous as shown

35   in most models – there are specific horizons within the crust where magma accumulation is favored,

36   while much of the crust remains melt-free.

37

38

INTRODUCTION

Magmatic systems are an integral part of the Earth engine. They feed eruptions to the surface; they lead to the formation of a wide range of ore deposits; they provide thermal energy for geothermal systems; and they are key to the differentiation and evolution of the Earth.

It is increasingly recognized that magmatic systems are vertically extensive, and they encompass much or the entirety of the crust, creating columns that are thermally anomalous and in which magma differentiation takes place (Bonin 2007; Sawyer et al. 2011; Annen et al. 2015; Bachmann and Huber 2016; Cashman et al. 2017). However, it is still poorly constrained how much magma exists at any given time, how it is distributed laterally and vertically, and how much of the crustal column is magma-free. Direct observation of current magmatic systems is limited by the relatively low resolution of geophysical methods (e.g., Magee et al. 2018; Cordell et al. 2022), and temporal variations over geological timescales can be significant (e.g., Giordano and Caricchi 2022) and are nonetheless inaccessible using direct observation.

Silicic volcanic eruptions are typically fed from shallow (100-300 MPa) magma bodies (Bégué et al. 2014b; Tramontano et al. 2017; Huber et al. 2019; among many others). In this sense, even though the pre-eruptive pressures of storage of silicic volcanics are increasingly better constrained, they give relatively little insight on the vertical extent of magmatic systems on the crustal scale.

Plutons – whose thicknesses span several kilometers – may seem to suggest vertically extensive magmatic systems; however, there is strong evidence that many or most plutons are built over relatively long timespans (hundreds of thousands to a few millions of years; e.g., Coleman et al. 2004; Samperton et al. 2015; Schaltegger et al. 2019; Eddy et al. 2022), and that the final products are amalgamations of diachronous magmatic events (see, for instance, Eddy et al. 2022; Wallrich et al. 2023), making it hard to identify the vertical distribution of magma within the crust at any given point in time. Further, understanding the depths at which magmas solidify to form plutons has proven challenging given the

63   limited set of geobarometers available that have sufficient precision to identify the true vertical extent of

64   magmatic systems.

65   Rhyolite-MELTS (Gualda et al. 2012) geobarometry offers new possibilities in this regard. Pre-eruptive

66   storage pressures (Gualda and Ghiorso 2014) are calculated using a glass composition to estimate the

67   pressure at which melt of that composition last equilibrated with the phenocryst assemblage observed in

68   the studied rock; they are particularly useful to determine the pressures of crystallization – or pre-

69   eruptive storage – of typically crystal-poor, melt-dominated magmas. In contrast, when whole-rock

70   compositions can be reliably assumed to closely reflect melt compositions, we can calculate extraction

71   pressures (Gualda et al. 2019), with which we estimate the depths at which these melts were segregated

72   from crystal-rich magma mush (see also Blundy 2022). To date, applications of this method of

73   determining extraction pressures have been restricted to volcanic rocks, revealing a complex record of

74   relatively shallow magma mushes in the Taupo Volcanic Zone, North Island, New Zealand (Gualda et al.

75   2019; Smithies et al. 2023) and in Hokkaido, Japan (Pitcher et al. 2021). In this work, we use whole-rock

76   compositions of selected plutonic rocks – which we infer to represent true melt compositions, as

77   discussed below – to reconstruct the magmatic system that gave rise to the studied plutons.

78   We use rocks from the northern Colorado River Extensional Corridor (CREC), Nevada, USA (Faulds et al.

79   2001; Miller and Miller 2002), particularly from the Aztec Wash Pluton (Falkner et al. 1995; Harper et al.

80   2004), from the Searchlight Pluton (Bachl et al. 2001) and its associated eruptives in the Highland Range

81   Volcanic Sequence (Faulds et al. 2002; Colombini et al. 2011; Wallrich et al. 2023), and from the Spirit

82   Mountain Batholith (Walker et al. 2007) to explore the distribution of melt-dominated magma and magma

83   mush as a function of depth in these magmatic systems. The CREC systems are ideally suited for a study

84   like this given that large (>10 km) crustal sections are exposed due to tectonic tilting. Further, these

85   systems have been the target of many detailed studies (see above), providing the necessary geological

86   and petrological background for our study.

87 The main granitic facies that make up these plutons show textural and compositional features that

88 suggest crystal accumulation and melt loss (Bachl et al. 2001; Harper et al. 2004; Walker et al. 2007),

89 making them unsuitable for estimation of rhyolite-MELTS extraction pressures. Instead, we take

90 advantage of fine-grained rocks that appear as dikes, sills, and marginal facies, which lack textural and

91 compositional features suggestive of crystal accumulation and melt loss. We also investigate medium-

92 grained leucocratic granites, at least some of which may record compositions representative of extracted

93 melts.

94 We use these data to infer magma distribution as a function of depth in these systems, and to refine our

95 ideas about the vertical extent of magmatic systems.

96 **GEOLOGICAL BACKGROUND**

97 **Colorado River Extensional Corridor**

98 The CREC (Figure 1) extends south from Las Vegas along the Colorado River, encompassing what is now

99 southernmost Nevada and parts of southeastern California and northwestern Arizona. It formed during a

100 major extensional episode in the Early to Middle Miocene that was accompanied by voluminous

101 magmatism spanning several million years as extension progressed from south to north (Faulds et al.

102 2001). Continued extension eventually led to tilting of crustal blocks that exposed steeply dipping cross

103 sections of plutons and volcanic sequences formed in the earlier phases of extension. We focus in this

104 paper on southern Nevada, where plutons are best exposed, specifically on the Spirit Mountain Batholith;

105 on Aztec Wash and Searchlight Plutons; and on silicic volcanic rocks in the Highland Range that are

106 associated with granites of the Searchlight Pluton.

107 **Aztec Wash Pluton**

108 The Aztec Wash Pluton (Figure 2) is a relatively small intrusion – with an exposed area of ~50 km^2 – that

109 intrudes diverse country rocks (Paleoproterozoic gneiss; Cretaceous granite; Early Miocene plutonic and

110   volcanic rocks of intermediate composition). Much of the pluton was tilted very steeply eastward during

111   extension, exposing a range of paleodepths of ~5 km (Harper et al. 2004), suggesting an original volume

112   on the order of ~300 km^3. Amphibole geobarometry indicates that the roof of the pluton was shallower

113   than ~6 km (Falkner et al. 1995; Patrick and Miller 1998). Based on zircon U-Pb and biotite $^{40}Ar/^{39}Ar$

114   dating, the pluton appears to have had a brief emplacement history, between 15.6 and 15.8 Ma (Falkner

115   et al. 1995; Cates et al. 2003; Leigh et al. 2018). The pluton comprises two main zones of roughly equal

116   areal extent: an interior Heterogeneous Zone and a relatively homogeneous Granite Zone that

117   interfingers with and overlies the Heterogeneous Zone (Falkner et al. 1995; Harper et al. 2004).

118   The Heterogeneous Zone is characterized by a succession of metric to decametric, fine-grained, mafic

119   sheets, intercalated with coarse-grained granite. The mafic sheets have common chilled margins, and the

120   underlying granite forms flame structures against the lower boundaries of the mafic sheets and granitic

121   pipes cut through the mafic sheets. This has been interpreted (Harper et al. 2004) as intrusion of mafic

122   magma within an evolving silicic magma body, primarily causing lateral flow of the mafic magmas at the

123   boundary between crystal-poor magma (i.e., melt-dominated magma) and crystal-rich magma (i.e.,

124   magma mush). Intermediate rocks with highly variable textures, interpreted to be hybrid mechanical and

125   chemical mixtures of the granitic and mafic magmas, are also abundant.

126   Very large (metric to decametric thickness, km-scale length), fine-grained, steeply-dipping granite sheets

127   intrude the Heterogeneous Zone. These are interpreted to be initially subhorizontal sills that intruded the

128   pluton after it was almost completely solidified, but prior to tilting (Miller et al. 2011).

129   In the Granite Zone, mafic sheets are absent. The dominant rocks are medium- to coarse-grained

130   granite. The coarser granite has a tight framework of centimetric feldspars with relatively little interstitial

131   material; quartz is almost entirely interstitial. The feldspars exhibit variable textures and zoning,

132   suggestive of different crystallization histories. Whole-rock compositions show enrichment in elements

133   that are compatible in feldspars and accessory minerals. For these reasons, these rocks have been

134   interpreted to have lost melt and concentrated crystals (i.e., they are cumulates) (Harper et al. 2004).

135   Medium-grained granite, in contrast, tends to have "looser" feldspar fabrics, with more prominent quartz.

136   Silica concentrations are higher and feldspar-compatible elements lower, suggesting that they

137   experienced less or no crystal concentration and melt loss.

138   The Granite Zone includes very fine-grained marginal rocks at the contact with country rocks. Rocks from

139   these marginal facies, which are interpreted to have been quenched, include both highly evolved

140   leucogranites (~77 wt.% SiO_2, very low compatible elements) and lower-SiO_2 granites. The compositions

141   of the lower-SiO_2, fine-grained marginal granites are very uniform and similar to the average composition

142   of the medium-grained Granite Zone granites and to the fine-grained sills that intrude the Heterogeneous

143   Zone. The lower-SiO_2 marginal microgranites are interpreted to be quenched manifestations of the felsic

144   magma parental to the rocks of the Granite Zone (Harper et al. 2004). Likewise, the almost identical late

145   sills are inferred to represent continuing input of the same magma (Miller et al. 2011). The high-silica

146   leucogranites, which are primarily concentrated at the roof (eastern margin), are interpreted to have

147   been melts extracted from Granite Zone cumulates (Harper et al. 2004).

148   **Spirit Mountain Batholith**

149   The Spirit Mountain Batholith (Figure 3), the largest intrusive body in the CREC, is a 40–50° west-tilted,

150   composite complex exposed over an area of ~250 km^2 (Volborth 1973; Faulds et al. 1992; Hopson et al.

151   1994; Howard et al. 1994; Haapala et al. 2005; Lowery Claiborne et al. 2006; Walker et al. 2007; Lang et

152   al. 2008). The host rocks include Paleo- and Mesoproterozoic gneiss and granite and a small Late

153   Cretaceous granite pluton. A section roughly 10 km in paleothickness is exposed from its roof downward,

154   with no exposed floor, leading to an estimated initial volume of well over 3000 km^3 for the batholith.

155   SHRIMP zircon U-Pb ages demonstrate that the batholith was constructed over a two million year period,

156   from ~17.4 to 15.3 Ma (Walker et al. 2007). This protracted period of granite emplacement contrasts

157   with the much shorter interval for Aztec Wash and Searchlight granite (~$\leq$0.2 Ma). Depth of

158   emplacement has not been well constrained before.

159   Walker et al. (2007) and Miller et al. (2011) suggest that more than 80% of the batholith, referred to as

160   Spirit Mountain granite, reflects a "patchwork" construction history during which granitic/rhyolitic magma

161   was repeatedly injected into crystal-rich mush. They infer that blurring of contacts between individual

162   intrusions was a consequence of destabilization of host mush. Melt extraction and accompanying mush

163   compaction resulted in an overall gradation from a ~2 km thick, highly fractionated leucogranite roof

164   zone, down through coarse, less silicic granite, and into coarse quartz monzonite, interpreted to be

165   cumulate, at deeper levels. Reversals of the downward trend toward coarser textures, better-defined

166   magmatic foliation, and lower silica, and rare well-defined internal contacts attest to repeated

167   replenishments. This complex construction history is supported by the zircon record: estimated ages of

168   final emplacement for samples within the Spirit Mountain granite unit span at least 1.5 Ma, from ~17.4 to

169   15.7 Ma. These ages are not uniformly distributed, and the leucogranite cap yield similar spreads in

170   estimated ages. All samples except a single 17.4 Ma granite have multiple age populations, in most cases

171   with a range similar to or in excess of 1 Ma. Walker et al. (2007) interpret the multiple populations to

172   reflect entrainment of antecrysts from within the system (elsewhere in Spirit Mountain mush, or from

173   deeper crustal levels).

174   Walker et al. (2007) divided the remaining rocks of the batholith into three principal units, all coeval with

175   to slightly younger than the younger portions of Spirit Mountain granite. All except for mafic sheets have

176   individual sample arrays of zircon ages similar to Sprit Mountain granite (spanning >1 Ma).

177   (1) Mirage Pluton (fine- to medium-grained, low-SiO_2 granite, ~16.0 Ma): discrete pluton, intrudes

178   relatively deep part of Spirit Mountain granite; it is locally separated from Spirit Mountain granite

179   by a septum of Proterozoic granite.

180   (2) Fine-grained granite (low-SiO_2 granite, ~15.9 Ma): compositionally very similar to Mirage Pluton,

181   texturally similar to fine-grained portions of Mirage Pluton rocks; it forms prominent west-dipping

182   (paleohorizontal) sheets (sills), pods, and more massive zones intruding Spirit Mountain granite

183   at a similar structural level to Mirage Pluton; blocks of Spirit Mountain granite are exposed with

184   massive fine-grained granite.

185   (3) Mafic sheets and pods (typically diorite, relatively low-volume but visually striking within the

186   granite batholith, ~16.0 Ma): sheets (initially subhorizontal) and pods in Spirit Mountain granite;

187   large blocks of the granite are engulfed within larger mafic bodies; they appear as both mingled

188   pillows and angular blocks within fine-grained granite.

189   **Searchlight Pluton**

190   The Searchlight Pluton (Figure 4) is also steeply dipping, with an exposed top-to-bottom section ~10 km

191   thick (~3-13 km, based on amphibole barometry; Bachl et al. 2001). Combined with its lateral extent of

192   13 km, this suggests an original volume of ~1000 km^3, making it considerably more voluminous than the

193   Aztec Wash Pluton, but smaller than the Sprit Mountain Batholith. It intruded Paleoproterozoic gneiss and

194   granite, Cretaceous granite, and, at its roof, a thick Miocene volcanic sequence. The pluton was emplaced

195   over a total interval that exceeded 1 Ma, from ~17.5 Ma (including small precursors) to 16.0 Ma; the

196   granitic (rhyolitic) portion of the pluton, however, was restricted to the final ~0.2 Ma portion of this

197   history (Cates et al. 2003; Eddy et al. 2022; Wallrich et al. 2023).

198   The pluton is subdivided into three units (Bachl et al. 2001): Lower, Middle, and Upper Searchlight Units.

199   The Lower Searchlight Unit is the thickest (~ 5 km thick), and zircon SHRIMP and CA-ID-TIMS ages

200   suggest a crystallization interval of ~16.2-16.8 Ma (Cates et al. 2003; Eddy et al. 2022). This unit

201   dominantly comprises medium- to coarse-grained quartz monzonite (59-70 wt.% SiO2; Bachl et al.

202   2001), and most rocks have very steep foliation that restores to subhorizontal prior to tilting. This fabric

203   is primary magmatic in the upper portion of the unit, but it is overprinted by tectonic fabric at deeper

204   levels.

205   The ~2 km thick Upper Searchlight Unit is composed of quartz monzonite that is similar to the Lower

206   Searchlight Unit in composition (63-71 wt.% SiO$_2$) and age (~16.2-16.6 Ma), but very distinct in texture.

207   It lacks foliation and is much finer grained, mostly equigranular, but with porphyry exposed near the roof

208   (Bachl et al. 2001).

209   Our work focuses on the ~2-3 km thick Middle Searchlight Unit, along with the rhyolitic portion of the

210   Upper Highland Range Volcanic Sequence (see below). The Middle Searchlight Unit intruded between the

211   Lower Searchlight and Upper Searchlight units between 16.0 and 16.2 Ma (Eddy et al. 2022). Except for

212   relatively sparse mafic magmatic enclaves and a single synplutonic, km-scale mafic lens, it is entirely

213   composed of granite. The dominant rocks, which comprise the lower ~90% of the unit, are coarse-

214   grained, low- to moderate-silica granites (69-75 wt.% SiO_2; Bachl et al. 2001). Rocks lower in this

215   coarse-grained sequence typically show a tight arrangement of feldspars with little interstitial material,

216   relatively low SiO_2, and compositions that suggest enrichment in elements compatible in feldspars and

217   accessory minerals. As in the case of the Aztec Wash Pluton, these rocks are interpreted to be cumulates.

218   The uppermost ~10% of the Middle Searchlight Unit is fine- to medium-grained leucogranite (76-78

219   wt.% SiO_2). The leucogranite is rich in incompatible elements and very poor in elements compatible in

220   feldspar and accessory minerals, which leads to the interpretation that it formed by extraction from

221   underlying cumulate mush (Bachl et al. 2001; Eddy et al. 2022; Wallrich et al. 2023).

222   Synplutonic, ~16.0 Ma microgranitic and rhyolitic dikes are common within the Middle and Upper

223   Searchlight units and the volcanic roof of the pluton (Hodge et al. 2006; Hinz et al. 2012; Wallrich et al.

224   2023). These dikes fall into two distinct groups: (1) phenocryst-rich rhyolite porphyry dikes with textures

225   and compositions very similar to those of the coarse-grained, low- to moderate-silica granites of the

226   Middle Searchlight Unit, from which they appear to emanate; and (2) slightly older, phenocryst-poor,

227   highly silicic dikes with compositions very similar to those of the leucogranite, which appears to be their

228   source (Wallrich et al. 2023).

229   **Highland Range Volcanic Sequence**

230   The Highland Range Volcanic Sequence (Figure 4) comprises >3 km of volcanic deposits, most of which

231   are interpreted to be correlative with the Searchlight Pluton (Faulds et al. 2002; Colombini et al. 2011;

232 Wallrich et al. 2023). The lower ~2 km portion of the sequence is composed of trachyandesites and

233 trachydacites thought to have been fed by the Lower and Upper units of the Searchlight Pluton. These

234 intermediate lavas are overlain by ~1 km of ~16.0 Ma rhyolite, dominantly phenocryst-poor, high-silica

235 tuffs and lavas that are inferred to have erupted from the Middle Searchlight Unit (Faulds et al. 2002;

236 Colombini et al. 2011; Wallrich et al. 2023). The stack of high-silica rhyolites is intruded by two small

237 plugs of rhyolite porphyry and capped by a lava flow that comprises both rhyolite porphyry and hybrid

238 lava interpreted to be mechanically mixed basaltic andesite and rhyolite (see Wallrich et al. 2023). This

239 composite lava is in turn capped by a series of basaltic andesite lavas that lack evidence for any silicic

240 input (Faulds et al. 2002).

241 The high-silica rhyolites are compositionally and texturally extremely similar to the phenocryst-poor highly

242 silicic dikes that emanate from the leucogranite of the Middle Searchlight Unit, and they are interpreted

243 to correlate with them (Wallrich et al. 2023). Likewise, the rhyolite porphyry plug and lava that are the

244 youngest silicic material in the Highland Range Volcanic Sequence are identical to the distinctive rhyolite

245 porphyry dikes that are the youngest intrusions in the Searchlight Pluton, and are therefore presumed to

246 be correlative (Wallrich et al. 2023). The high-silica rhyolites, like the phenocryst-poor dikes, have been

247 interpreted as magma extracted from the leucogranite sheet at the top of the Middle Searchlight Unit.

248 The rhyolite porphyries (dikes, plugs, and lava) are inferred to represent mush remobilized from the

249 lower part of the Middle Searchlight Unit and extracted and erupted along with injections of basaltic

250 andesite magma as the final episode related to termination of activity within the Searchlight Pluton

251 (Wallrich et al. 2023).

252 **Late silicic dike swarms**

253 The final intrusive manifestation of the silicic magma systems was intrusion of the Eldorado and

254 Newberry dike swarms shortly after final solidification of the plutons (Falkner et al. 1995; Bachl et al.

255 2001; George et al. 2005; Walker et al. 2007; Hinz et al. 2012). The former swarm intruded both

256 Searchlight and Aztec Wash plutons, and the latter the Spirit Mountain batholith. The two swarms are

257   very similar: both are north-striking and emplaced ~15.3-15.6 Ma and dominated by large (3-20 m thick),

258   porphyritic microgranite/rhyolite dikes. Thinner andesite dikes are subordinate. The silicic dikes are

259   almost indistinguishable in elemental composition and have similar phenocryst assemblages (sanidine +

260   plagioclase + biotite + amphibole + titanite + apatite + FeTi oxides + zircon $\pm$ quartz). The only

261   significant difference between the two swarms is that Newberry dikes have prominent quartz

262   phenocrysts, whereas quartz phenocrysts have not been observed in Eldorado dikes.

263   **METHODS**

264   **Data used**

265   We use elemental data for Aztec Wash Pluton (whole rock, Harper et al. 2004), Searchlight Pluton

266   (whole-rock, Bachl et al. 2001), Spirit Mountain batholith (whole-rock, Walker et al. 2007), and the

267   Highland Range Volcanic Sequence (whole-rock and glass, Colombini et al. 2011; Wallrich et al. 2023). A

268   few additional glass compositions were obtained for high-silica rhyolites from the Highland Range

269   Volcanic Sequence, using identical procedures as in Gualda et al. (2022). All compositions used are listed

270   in Table 1.

271   **Geobarometry approach**

272   This study focuses on obtaining pressure estimates based primarily on whole-rock compositions from the

273   Aztec Wash and Searchlight plutons, the Spirit Mountain Batholith, and from the Highland Range Volcanic

274   Sequence, with additional geobarometric estimates using glass compositions from a subset of rocks from

275   the latter. While the procedures used to obtain pressures (i.e., projection onto the haplogranitic ternary

276   and rhyolite-MELTS geobarometry) are nearly identical for all compositions used, the assumptions and

277   interpretations involved differ significantly.

278   Geobarometry using glass compositions yields what we refer to as "pre-eruptive storage pressures" (see

279   also Gualda and Ghiorso 2014) (Figure 5). The critical assumption is that a melt of composition given by

280   the analyzed glass equilibrated with an assemblage consisting of the phenocrysts present in the rock. For

281   rocks erupted explosively, syneruptive crystallization is limited or absent, such that pressures are

282   interpreted to represent the crustal levels at which magma was last stored prior to eruption. Glass-

283   bearing rocks studied here are crystal-poor, lacking evidence of widespread disequilibrium features (e.g.,

284   dissolution features, mottled textures, etc.), suggesting equilibration of observed phenocrysts with the

285   melt. As demonstrated previously (Gualda and Ghiorso 2014; Bégué et al. 2014b; Pamukcu et al. 2015),

286   rhyolite-MELTS is very sensitive to the quality of the glass composition used, and it can often be used to

287   filter out altered compositions or compositions that did not equilibrate with the observed mineralogy.

288   Glass-bearing rocks investigated here all contain phenocrysts of quartz, sanidine, and plagioclase – thus,

289   we focus on an assemblage involving quartz and two feldspars (aka Q2F). In some cases, we also

290   consider the presence of magnetite and ilmenite (aka Q2FMI; see below), which are ubiquitously

291   observed in the studied rocks.

292   Geobarometry using whole-rock compositions yields what we refer to as "extraction pressures" (see

293   Gualda et al. 2019) (Figure 5). In this case, the critical assumption is that the whole-rock composition

294   very closely approximates a true melt composition – this melt equilibrated with and was extracted from

295   an inferred crystal assemblage. Further, we assume that nearly pure melt is extracted (i.e., negligible

296   amounts of crystals entrained during extraction), such that the whole-rock composition represents the

297   composition of the melt. While this latter assumption is probably never strictly true, the assumption is

298   relaxed by the fact that the concentration of crystals entrained during extraction would have to be large

299   enough to modify the major-element composition of the whole-rock. In this sense, sparse crystals can be

300   included during extraction without significantly modifying the whole-rock composition. Further, refractory

301   accessory minerals, such as zircon, can be effectively neglected, given that the calculations are not

302   sensitive to the Zr (and other trace-element) concentration of the melt. Importantly, given that extraction

303   pressures record the pressure at which a melt last equilibrated with a crystal-rich residue (the launching

304   point of Blundy 2022), they do not record the level of emplacement of such magmas – instead, they

305   record the pressures at which magma mushes exist in the crust. We use geochemical and petrographic

13

306 evidence (i.e., Harper et al. 2004; Walker et al. 2007; Wallrich et al. 2023) to distinguish rocks that may

307 correspond to melts from those that likely experience melt loss and crystal accumulation. Further, we

308 leverage the sensitivity of rhyolite-MELTS to the quality of the input composition to filter out compositions

309 that cannot be considered to correspond to a melt that equilibrated with an assemblage consisting of

310 quartz and two feldspars (±magnetite, ±ilmenite). In the case of extraction pressures, the assemblage

311 with which the melt last equilibrated cannot be directly observed and it has to be inferred (see Gualda *et*

312 *al.* 2019); rocks in the CREC ubiquitously have plagioclase and alkali feldspar present, and it is hard to

313 envision that extraction would have taken place from either plagioclase-free or alkali feldspar-free rocks.

314 The presence of quartz in the extraction assemblage is less certain. Interestingly, rhyolite-MELTS

315 calculations allow us to test whether quartz is likely to be present in the extraction assemblage, in

316 addition to plagioclase and alkali feldspar (see below).

317 **Haplogranitic projection geobarometry**

318 We use the haplogranitic projection of Blundy & Cashman (2001) to yield rough estimates of pressures

319 using the compositions employed in this study. While work to date has focused on glass compositions and

320 storage pressures (Blundy and Cashman 2001; Gualda and Ghiorso 2013a, b; Bégué et al. 2014a; Gualda

321 et al. 2022), it is possible to obtain extraction pressures using the same approach. Rocks studied here are

322 part of a magmatic sequence from typical metaluminous mafic magmas to slightly peraluminous high-

323 silica magmas (Cawthorn and Brown 1976), for which the projection scheme of Blundy & Cashman

324 (2001) is very well suited. We use a Microsoft Excel template created by us to perform the projection

325 from the initial compositions, following the procedures described in Blundy & Cashman (2001). We

326 compare the position of the projected data to the position of the experimentally determined

327 quartz+feldspar cotectic curves to roughly assess pre-eruptive storage and extraction pressures.

328   **Rhyolite-MELTS geobarometry**

329   All rhyolite-MELTS calculations are performed using MELTS_Excel (Gualda and Ghiorso 2015). Extraction

330   pressure calculations – using whole-rock compositions – are performed with pressures between 500 and

331   100 MPa in 25 MPa steps. Pre-eruptive storage pressure calculations – using glass compositions – are run

332   between 400 and 25 MPa in 25 MPa steps. The larger pressure interval used for extraction pressures

333   (500-25 MPa) was chosen simply because extraction pressures tend to generally extend to deeper

334   pressures than pre-eruptive storage pressures. For all pressure calculations, temperatures used are

335   between 1100 and 700 °C in 1 °C steps. We buffer oxygen fugacity at the Ni-NiO (NNO) buffer, which is

336   particularly suitable given the presence of the TMQAI (titanite, magnetite, quartz, amphibole, ilmenite)

337   buffering assemblage (Wones 1989) in these rocks. We thus search for quartz-2 feldspar (Q2F) pressures

338   (Gualda and Ghiorso 2014), but also for pressures that satisfy the condition of simultaneous equilibration

339   between quartz, two feldspars, magnetite and ilmenite (Q2FMI pressures). The procedure used here to

340   search for a 5-phase solution (see Figure 6) is an extension of the methods developed by Gualda &

341   Ghiorso (2014), similar to the one used in Foley et al. (2020). When Q2FMI pressures are found (see

342   Figure 6a), those are reported; if no Q2FMI pressure is obtained, but a Q2F pressure is found, the Q2F

343   pressure is reported (see Figure 6b); if neither is found (see Figure 6c-d), we conclude that no suitable

344   pressures can be estimated. As demonstrated by Gualda & Ghiorso (2014) and Ghiorso & Gualda (2015),

345   water abundance does not play a critical role in pressure determinations for Q2F pressures; we thus use

346   enough water (>12 wt.%) to ensure water saturation at all pressures.

347   **Magma evolution calculations using Rhyolite-MELTS**

348   Extraction pressures reveal the crustal levels from which melts separate from crystal-rich magma mush;

349   we emphasize that multiple extraction levels are possible in a putative transcrustal magmatic system.

350   Magmas extracted from mush can be transported vertically through the crust and stored at shallower

351   levels, where they can lose heat and solidify. We simulate this solidification process by considering

352   various plausible crustal levels to which extracted magmas could have been transported. To do so, we

353 perform isobaric cooling sequence calculations with rhyolite-MELTS (Gualda et al. 2012) with all whole-

354 rock compositions that return extraction pressures deeper than 175 MPa. For the cases in which the

355 extraction pressure is deeper than 300 MPa, calculations are performed at 240, 200, 160, and 120 MPa;

356 when the extraction pressure is between 175 and 300 MPa, calculations are only performed at 160 and

357 120 MPa. All calculations are performed from the liquidus to 10 wt.% liquid in 1 °C steps. We assume

358 water saturation during extraction and pre-eruptive storage, and thus include enough water for

359 saturation at the liquidus. The water-saturated liquidus is determined using MELTS_Excel for each

360 combination of composition and pressure, and the calculation is interrupted when the liquid content goes

361 below 10 wt.%, at which point the rhyolitic near-invariant has typically been reached for the compositions

362 used in this study. A total of 96 such simulations is presented here.

363 **RESULTS & DISCUSSION**

364 **Whole-rock and glass compositions**

365 Whole-rock compositions for the systems studied here (Aztec Wash, Middle Searchlight-Upper Highland

366 Range, Spirit Mountain systems) show relatively simple relationships in Harker diagrams (Figure 7), most

367 evidently displayed by decreasing FeO, MgO, CaO, and TiO_2 with increasing SiO_2. Values for Na_2O

368 decrease slightly while K_2O increases sightly with increasing SiO_2. Compositions from all three systems fall

369 into three categories (see Figure 7):

370 Group 1: Rocks with SiO_2 < 72.0 wt.%; these rocks are coarse-grained, and they have textural

371   features consistent with crystal accumulation and melt loss; they make up a significant

372   fraction of the granitic rocks found in all three plutons.

373 Group 2: Rocks with SiO_2 between 72.0 and 74.5 wt.%; this group includes granitic rocks in which

374   cumulatic textures and compositional traits are not as pronounced; importantly, rocks in this

375   group include fine-grained marginal facies in the Aztec Wash Pluton and dikes and sills

376   intruding all three plutons that lack textural or chemical evidence for crystal accumulation.

377   Group 3: Rocks with SiO$_2$ > 75.5; these rocks include facies along the upper margin (i.e., the roof) of

378   the Aztec Wash Pluton, leucogranite that forms the upper part of the Middle Searchlight Unit

379   and the Spirit Mountain Batholith, phenocryst-poor dikes that cross-cut the leucogranite and

380   Upper Searchlight Unit, and the high-silica rhyolites in the Highland Range Volcanic

381   Sequence. We note that there is a subgroup within this group characterized by more evolved

382   compositions with relatively high silica (>76.5 wt.% SiO$_2$) and low FeO (<1.0 wt.%) and MgO

383   (<0.25 wt.%).

384   Glass compositions for rocks from the Highland Range Volcanic Sequence (orange crosses in Figure 7) fall

385   within group 3.

386   The compositional relationships described above are used by Harper et al. (2004), in the case of the

387   Aztec Wash Pluton, to suggest that group 1 are cumulates (Granite Zone Cumulate Unit). Granites of

388   what they refer to as the Granite Zone Transitional Unit have group 2 compositions and textures,

389   suggesting limited or no crystal accumulation. We emphasize that the number of whole-rock compositions

390   per group presented in Harper et al. (2004) and discussed here does not in any way represent the

391   volumetric abundances of these units – specifically, marginal facies and dikes (groups 2 and 3) have been

392   analyzed to a disproportionately high degree due to their potential petrological significance.

393   The relationship between TiO$_2$ and SiO$_2$ for rocks from the Aztec Wash Pluton (Figure 8a) displays well

394   the concept advanced by Harper et al. (2004): the presumed input magma has a composition that is

395   intermediate between that of the most obvious cumulates (high TiO$_2$, low SiO$_2$) and fractionates (low

396   TiO$_2$, high SiO$_2$). The same relationship is observed with P$_2$O$_5$, Zr, Hf, Eu, and LREE, while the reverse

397   relationship (i.e., positive correlation with SiO$_2$) is seen for Rb. While we do not have as large a number

398   of trace elements available for rocks from the Middle Searchlight Unit, similar relationships are seen

399   between SiO$_2$, TiO$_2$, and Zr (Figure 8b). We thus extend the concept advanced by Harper et al. (2004) to

400   the Middle Searchlight-Upper Highland Range Magmatic System. The same also applies to the Spirit

401   Mountain Batholith (Figure 8c). In essence, magmas with compositions that fall within group 2 fed all

402   three systems; separation of crystal-poor, melt-dominated magma from crystal-rich magma mush led to

403   the formation of high-silica magmas (group 3). It is possible that magmas from group 3 formed their own

404   magma mushes at shallower levels – this possibility will be discussed in greater detail below.

405   Importantly, the similarity in composition between glass in rocks from the Upper Highland Range Volcanic

406   Sequence and leucogranites from the Middle Searchlight Unit shows that whole-rock compositions from

407   group 3 are viable melt compositions.

408   **Extraction and pre-eruptive storage pressures**

409   For magmas saturated in quartz and two feldspars, there is a strong correlation between SiO_2 and

410   pressure (Blundy and Cashman 2001; Gualda and Ghiorso 2013b, 2014; and references therein). As

411   expected, we see a strong correlation between pressure of extraction or pre-eruptive storage and the

412   groups identified above (Figure 9, Figure 10), except that group 3 can be subdivided into two subgroups:

413   Group 1:   None of these compositions yields a viable extraction pressure.

414   Group 2:   Extraction pressures are all Q2F (15 compositions), in the range of 370-450 MPa.

415   Group 3a: Extraction pressures are mostly Q2FMI (11 compositions), with five Q2F pressures,

416   covering the pressure range of 185-300 MPa; two glass compositions yield Q2FMI storage

417   pressures.

418   Group 3b: Extraction pressures are mostly Q2FMI (12 compositions), with one Q2F pressure, covering

419   the range of 120-180 MPa; glass compositions (orange crosses) yield five Q2FMI and four

420   Q2F storage pressures, mostly in the 120-150 MPa range (4 compositions), with one

421   additional value of ~90 MPa.

422   The extraction and pre-eruptive storage pressures we present here broadly define three main horizons

423   within the crust where magma was present (Figure 11). The first one spanned a depth range of ~13.5-

424   16.5 km (assuming a crustal density of $2.7*10^3$ kg/m^3), suggesting a ~3 km thick mush zone, which

18

425   cannot be directly observed in the field given the current level of exposure of the crust (i.e., at none of

426   the three complexes is the crust exposed to such deep levels).

427   A gap in extraction pressures is very distinct between this and the next group, suggesting that there was

428   a region with thickness greater than ~4 km where little or no magma was present. We note that the

429   pressure gap (110 MPa) is much larger than the uncertainty associated with the rhyolite-MELTS

430   geobarometer (<25 MPa, 1-sigma; see Gualda and Ghiorso 2014; Pitcher et al. 2021; Pamukcu et al.

431   2021), lending confidence to the idea of a significant region in the crust with little to no melt at the time.

432   In fact, these depths correspond to the location of the Lower Searchlight Unit, which is inferred –

433   particularly from geochronology data (Eddy et al. 2022; Wallrich et al. 2023) – to have been completely

434   solid at the time of emplacement and crystallization of the Middle Searchlight Unit.

435   The distribution of magma at shallower levels differs slightly for the three magmatic systems studied (see

436   Figure 9, Figure 11). For the Aztec Wash Pluton (see Figure 9, Figure 11b), there was very good

437   separation between two magma-bearing regions. One of these regions occupied pressures between 190

438   and 240 MPa (~7.0 and 9.0 km depth; one value at 280 MPa and ~10.5 km), suggesting a ~2.0 km thick

439   magmatically active region. Most of the melt-dominated magma that formed the high-silica marginal

440   facies in the Aztec Wash pluton derived from this horizon. A smaller gap (~40 MPa, ~1.5 km) separated

441   this magma-bearing horizon from the next one. The topmost magma-bearing region we can infer from

442   these data spanned a depth range from 4.5 to 6.0 km, revealing a ~1.5 km thick magma-bearing region.

443   Extraction pressures for the Middle Searchlight-Upper Highland Range Magmatic System (see Figure 9,

444   Figure 11c) reveal a similar but more patchy distribution of magma, spanning from 180 to 310 MPa

445   (~6.5-11.5 km depth); three clusters are seen, but a larger number of samples would be needed to

446   confirm the distribution in detail. This corresponds to the most voluminous portion of the Middle

447   Searchlight-Upper Highland Range Magmatic System. Extraction and storage pressures form a contiguous

448   cluster at pressures from 160 and 120 MPa (~4.5-6.0 depth; one storage pressure of ~90 MPa, ~3.5 km

449   depth), revealing a ~1.5 km thick magma-bearing region very similar to that observed in the Aztec Wash

450   Magmatic System. Interestingly, most pre-eruptive storage pressures appear in this cluster, showing that

451   magmas that erupted to form the high-silica rhyolite pyroclastic unit(s) in the Highland Range Volcanic

452   Sequence were stored at this level. It is interesting, however, that extraction pressures are also found

453   within this horizon, demonstrating that magma mush must have existed at this depth range as well.

454   For the Spirit Mountain Batholith (see Figure 9, Figure 11d), extraction pressures suggest a single

455   magma-bearing region at pressures of 130-220 MPa (~5.0-8.0 km depth), without a noticeable gap as

456   seen at the Aztec Wash, and without the clustering seen in the Middle Searchlight-Upper Highland Range

457   Systems.

458   Despite these small differences, the distribution of pressures we see (Figure 11) strongly suggests a non-

459   uniform distribution of magma as a function of depth for all systems studied. In combination, our

460   pressure results suggest two to three discrete magma-bearing regions, separated from each other by

461   regions that seem magma-poor or magma-free. It is remarkable that the results for the three magmatic

462   systems are very similar, lending confidence to the interpretations made here. The reasons why magmas

463   stall at these depths deserve further investigation.

464   **Magma differentiation**

465   The identification of three distinct magma-bearing horizons with different compositions raises important

466   questions about how magma differentiation is coupled with pre-eruptive storage, extraction, and ascent.

467   One possibility is that magmas of groups 3a and 3b were formed by fractional crystallization of magmas

468   of group 2 that stalled at different levels. We test this hypothesis by performing isobaric cooling

469   sequences for magmas with compositions given by rocks of group 2 at pressures of 240, 200, 160, and

470   120 MPa (Figure 12a, Figure 13). The assumption is that magmas were potentially transported to these

471   levels and solidified until extraction took place. Because extraction and storage assemblages invariably

472   include quartz and two feldspars (i.e., they are all either Q2F or Q2FMI pressures), extraction should take

473   place at the rhyolitic near-invariant (see Gualda et al. 2012) for each combination of composition and

474   pressure. In Figure 12a, the red triangles represent the silica content of the near-invariant for each

475   composition at each pressure. We observe that melts with compositions from group 2 can generate silica

476   contents consistent with what is observed in group 3a, through differentiation at pressures between

477   ~200-240 MPa. However, it is also clear that solidification of magmas from group 2 at pressures of 120

478   and 160 MPa does not generate compositions that are enriched enough in silica to give rise to magmas of

479   group 3b. While we show that it is likely that magmas from group 3a were derived from differentiation of

480   magmas with compositions equivalent to those of group 2, we also demonstrate that it is unlikely that

481   magmas from group 3b were derived directly from these same magmas.

482   We turn our attention to the possibility that magmas from group 3b were derived, instead, from magmas

483   with compositions equivalent to those from group 3a. We test this hypothesis by performing isobaric

484   cooling sequences for magmas with compositions given by rocks of group 3a at pressures of 160 and 120

485   MPa. In Figure 12b, the red triangles again represent the position of the rhyolitic near-invariant. Our

486   simulations show that solidification of magmas with compositions equivalent to group 3a leads to silica

487   contents that are higher by up to 0.5 wt.% SiO_2 relative to the cases in which we used initial

488   compositions equivalent to group 2. The more evolved compositions resulting from solidification of

489   magmas with compositions equivalent to group 3a much more closely match the compositions of rocks

490   from group 3b. We conclude that group 3b magmas were not derived directly from group 2 magmas;

491   rather, they are the products of differentiation of magmas from group 3a.

492   One important point that is not apparent in Figure 12 relates to the amount of time that a given parcel of

493   magma resides at the near-invariant. Magmas with compositions equivalent to group 2 need to attain

494   crystal contents of 12 to 27 wt.% crystals, depending on pressure (e.g., lower values for deeper

495   conditions), to reach the near-invariant (see Figure 13). From that point onward, solidification proceeds

496   essentially isothermally (see Gualda et al. 2012), which means that magmas are stuck at those conditions

497   for extended periods of time, enhancing the opportunity of extraction of crystal-poor, melt-dominated

498   magma from mush (see Dufek and Bachmann 2010). The same is observed for starting compositions

499   from group 3a (Figure 13), except that the amount of solidification necessary to reach the near-invariant

500   is smaller (2-7 wt.% crystals), which is explained by the smaller difference in pressure between groups

501   3a and 3b, causing a smaller difference in the position of the near-invariant in this case (see Figure 13).

502   We conclude that differentiation took place in a stepwise manner (Figure 14). Relatively low-silica (72-

503   74.5 wt.% SiO_2) magmas were extracted at deeper levels (13.5-16.5 km, 370-440 MPa) and they stalled

504   at intermediate levels (7.0-9.5 km, 185-255 MPa). At those levels, differentiation led to melts with silica

505   content in the 76-77 wt.% range. Magmas extracted from these intermediate levels fed eruptions at the

506   surface, but they also stalled at shallower levels (4.5-6.0 km, 120-160 MPa) – differentiation of these

507   magmas gave rise to rhyolites with even higher silica (>77 wt.% SiO_2). These rhyolites fed eruptions

508   themselves, but they also solidified to form high-silica granites in the subsurface. In the CREC, we do not

509   find evidence for shallower magma pre-eruptive storage – if any further fractionation took place,

510   extracted melt remained in close proximity to mush (contiguous extraction in the sense of Gualda et al.

511   2019), and the difference in composition between fractionated melts and their host cumulates must have

512   been small to undetectable.

513   **IMPLICATIONS**

514   For nearly 20 years, the so-called "Mush Model" (Bachmann and Bergantz 2004; see also Hildreth 2004)

515   has dominated our understanding of the origin and evolution of high-silica rhyolites. The concept

516   advanced by Bachmann & Bergantz (2004) presumes the existence of a dacitic magma body, from which

517   melt-dominated magma of rhyolitic composition is extracted, in situ, from a crystal-rich mush – high-silica

518   rhyolites can erupt to the surface from such reservoirs. While the "Mush Model" is simple and elegant, it

519   has the limitation that a single magma body – consisting of magma mush in contact with melt-dominated

520   magma – exists, and its connections with other crustal levels is not entirely clear.

521   In contrast, the last 10-15 years have seen the emergence of the idea of transcrustal magmatic systems

522   (Bonin 2007; Sawyer et al. 2011; Annen et al. 2015; Bachmann and Huber 2016; Cashman et al. 2017).

523   This view of magmatic systems emphasizes that the thermal anomalies associated with the presence of

524   magmas are not limited to specific crustal depths, but that they must encompass much or all of the crust.

525 The challenge, in this case, is to understand the distribution of magmas as a function of depth – it seems

526 unlikely that magma will be present over the whole thickness of the crust at all times through the life of a

527 magmatic system; however, obtaining data that can provide direct evidence for the distribution of

528 magma as a function of depth has proven challenging.

529 In our view, our work provides an important bridge between these two perspectives. Our extraction and

530 pre-eruptive storage pressures reveal multi-tiered systems consisting of two or three crustal levels in

531 which magma is present. As it turns out, the transcrustal magmatic systems of the CREC were made of

532 discrete horizons in which magma was present, with others that were magma-poor or magma-free.

533 Importantly, in each of the magma-rich horizons, differentiation took place along the lines of what is

534 proposed by Bachmann & Bergantz (2004). However, the extent of differentiation in each tier or horizon

535 was much smaller than what Bachmann & Bergantz (2004) originally envisioned (i.e., from dacite directly

536 to high-silica rhyolite). Instead, we infer that rhyolites with relatively low silica contents (i.e., 72.0-74.5

537 wt.%) were extracted at mid-crustal levels (~13.5-16.5 km); rhyolite magmas with intermediate to high

538 silica contents (i.e., 75.5-77.5 wt.%) were extracted at shallower crustal levels of the crust (~7.0-9.5

539 km); and, finally, rhyolites with the highest silica contents (i.e., 77.5-78.0 wt.%) were extracted at the

540 shallowest levels (~4.5-6.0 km). This reveals that differentiation took place in a stepwise manner. This

541 subtle difference is important in at least two ways.

542 First, a longstanding problem in petrology has been the apparent paucity of rocks that can be

543 unambiguously interpreted as cumulates (Wiebe 1994; Deering and Bachmann 2010; Glazner et al. 2015;

544 Lee and Morton 2015; Keller et al. 2015; Barnes et al. 2019). In the multi-tiered differentiation model we

545 propose, the extent of differentiation in each step is limited. This means that the cumulatic signatures

546 that would be expected are rather muted, particularly because the most evident signatures are expected

547 in the extracted liquids, rather than in the residual cumulates (see Deering and Bachmann 2010). In this

548 sense, ordinary granites become good candidates for the cumulates left behind after melt extraction. The

549 fact that they do not show extreme cumulatic signatures only means that the extent of differentiation

550   that leads to the formation of such cumulatic granitoids is appropriately small (consistent with mass-

551   balance models of Wallrich et al. 2023).

552   Further, our data show that melt-dominated magma can be repeatedly mobilized from crystal mush. It is

553   somewhat troubling that we still do not understand well the mechanisms whereby melt separates

554   efficiently from mush at rapid (probably centennial to millennial) timescales (see Bachmann and Huber

555   2019). Nonetheless, the very existence of voluminous crystal-poor volcanic rocks demonstrates

556   unambiguously that separation of melt from mush can be a very efficient process. It is also important to

557   emphasize that while extracted magmas can erupt to the surface, just as commonly, extracted magmas

558   find shallower crustal levels where they stall and differentiate. The reasons why rising magma would stall

559   rather than continue to the surface are also not well understood and deserve further study. Yet, the idea

560   of a crustal-scale magmatic system effectively makes it necessary for such multi-staging history to take

561   place.

562   In summary, what we propose is a multi-stage magma differentiation column, which also represents a

563   thermal anomaly within the crust. This column is made of several discrete horizons in which magma is

564   present, and several magma-free regions. The silica content of extracted melts is effectively buffered at a

565   given depth (pressure) by the dependency of the position of the rhyolitic near-invariant as a function of

566   pressure (Blundy and Cashman 2001; Gualda and Ghiorso 2013b). What results is a system in which

567   variation in silica content of melts is incremental, and the major-oxide signatures showing accumulation

568   of crystals are intrinsically limited. With the benefit of hindsight, this model may seem almost too

569   obvious. However, direct evidence in the level of detail presented here has been lacking. We need to

570   better understand the processes of separation of melt from mush, as well as the controls on the vertical

571   vs lateral motion of magmas in the shallow crust.

576 **DATA AVAILABILITY STATEMENT**

577 The data underlying this article are available in the article and in its online supplementary material.

578   **REFERENCES**

579   Annen C, Blundy JD, Leuthold J, Sparks RSJ (2015) Construction and evolution of igneous bodies:
580   Towards an integrated perspective of crustal magmatism. Lithos 230:206–221.
581   https://doi.org/10.1016/j.lithos.2015.05.008

582   Bachl CA, Miller CF, Miller JS, Faulds JE (2001) Construction of a pluton: Evidence from an exposed cross
583   section of the Searchlight pluton, Eldorado Mountains, Nevada. Geological Society of America
584   Bulletin 113:1213–1228

585   Bachmann O, Bergantz GW (2004) On the origin of crystal-poor rhyolites: Extracted from batholithic
586   crystal mushes. Journal of Petrology 45:1565–1582. https://doi.org/10.1093/petrology/egh019

587   Bachmann O, Huber C (2016) Silicic magma reservoirs in the Earth's crust. American Mineralogist
588   101:2377–2404. https://doi.org/10.2138/am-2016-5675

589   Bachmann O, Huber C (2019) The Inner Workings of Crustal Distillation Columns; the Physical
590   Mechanisms and Rates Controlling Phase Separation in Silicic Magma Reservoirs. Journal of
591   Petrology 60:3–18. https://doi.org/10.1093/petrology/egy103

592   Barnes CG, Werts K, Memeti V, Ardill K (2019) Most Granitoid Rocks are Cumulates: Deductions from
593   Hornblende Compositions and Zircon Saturation. Journal of Petrology 60:2227–2240.
594   https://doi.org/10.1093/petrology/egaa008

595   Bégué F, Deering CD, Gravley DM, et al (2014a) Extraction, Storage and Eruption of Multiple Isolated
596   Magma Batches in the Paired Mamaku and Ohakuri Eruption, Taupo Volcanic Zone, New Zealand.
597   Journal of Petrology 55:1653–1684. https://doi.org/10.1093/petrology/egu038

598   Bégué F, Gualda GAR, Ghiorso MS, et al (2014b) Phase-equilibrium geobarometers for silicic rocks based
599   on rhyolite-MELTS. Part 2: application to Taupo Volcanic Zone rhyolites. Contributions to
600   Mineralogy and Petrology 168:. https://doi.org/10.1007/s00410-014-1082-7

601   Blundy J (2022) Chemical Differentiation by Mineralogical Buffering in Crustal Hot Zones. Journal of
602   Petrology 63:egac054. https://doi.org/10.1093/petrology/egac054

603   Blundy J, Cashman K (2001) Ascent-driven crystallisation of dacite magmas at Mount St Helens, 1980-
604   1986. Contrib Mineral Petrol 140:631–650

605   Bonin B (2007) A-type granites and related rocks: Evolution of a concept, problems and prospects. Lithos
606   97:1–29. https://doi.org/10.1016/j.lithos.2006.12.007

607   Cashman KV, Sparks RSJ, Blundy JD (2017) Vertically extensive and unstable magmatic systems: A
608   unified view of igneous processes. Science 355:1280-+. https://doi.org/10.1126/science.aag3055

609   Cates NL, Miller JS, Miller CF, et al (2003) Longevity of plutonic systems: SHRIMP evidence from Aztec
610   Wash and Searchlight plutons, Nevada. In: Geological Society of America, abstracts with
611   programs. pp 1346–53

612   Cawthorn RG, Brown PA (1976) A Model for the Formation and Crystallization of Corundum-Normative
613   Calc-Alkaline Magmas through Amphibole Fractionation. The Journal of Geology 84:467–476

614 Coleman D, Gray W, Glazner A (2004) Rethinking the emplacement and evolution of zoned plutons:
615   Geochronologic evidence for incremental assembly of the Tuolumne Intrusive Suite, California.
616   Geology 32:433–436. https://doi.org/10.1130/G20220.1

617 Colombini LL, Miller CF, Gualda GAR, et al (2011) Sphene and zircon in the Highland Range volcanic
618   sequence (Miocene, southern Nevada, USA): elemental partitioning, phase relations, and
619   influence on evolution of silicic magma. Mineralogy and Petrology 102:29–50.
620   https://doi.org/10.1007/s00710-011-0177-3

621 Cordell D, Hill G, Bachmann O, et al (2022) Estimating melt fraction in silicic systems using Bayesian
622   inversion of magnetotelluric data. Journal of Volcanology and Geothermal Research 423:107470.
623   https://doi.org/10.1016/j.jvolgeores.2022.107470

624 Deering CD, Bachmann O (2010) Trace element indicators of crystal accumulation in silicic igneous rocks.
625   Earth and Planetary Science Letters 297:324–331. https://doi.org/10.1016/j.epsl.2010.06.034

626 Dufek J, Bachmann O (2010) Quantum magmatism: Magmatic compositional gaps generated by melt-
627   crystal dynamics. Geology 38:687–690. https://doi.org/10.1130/g30831.1

628 Eddy MP, Pamukçu A, Schoene B, et al (2022) Constraints on the timescales and processes that led to
629   high-SiO2 rhyolite production in the Searchlight pluton, Nevada, USA. Geosphere 18:1000–1019.
630   https://doi.org/10.1130/GES02439.1

631 Falkner CM, Miller CF, Wooden JL, Heizler MT (1995) Petrogenesis and tectonic significance of the calc-
632   alkaline, bimodal Aztec Wash pluton, Eldorado Mountains, Colorado River extensional corridor. J
633   Geophys Res 100:10453–10476. https://doi.org/10.1029/94JB03357

634 Faulds JE, Feuerbach DL, Miller CF, Smith EI (2001) Cenozoic evolution of the northern Colorado River
635   extensional corridor, southern Nevada and northwest Arizona. Pacific Section of the American
636   Association of Petroleum Geologists Publication GB 78:

637 Faulds JE, Geissman JW, Shafiqullah M (1992) Implications of paleomagnetic data on Miocene extension
638   near a major accommodation zone in the Basin and Range Province, northwestern Arizona and
639   southern Nevada. Tectonics 11:204–227. https://doi.org/10.1029/91TC00869

640 Faulds JE, Olson EL, Harlan SS, McIntosh WC (2002) Miocene extension and fault related folding in the
641   Highland Range, southern Nevada: a three-dimensional perspective. Journal of Structural
642   Geology 24:861–886

643 Foley ML, Miller CF, Gualda GAR (2020) Architecture of a super-sized magma chamber and remobilization
644   of its basal cumulate (Peach Spring Tuff, USA). Journal of Petrology in press

645 George BE, Miller CF, Walker BA, Wooden JL (2005) Newberry Mountains Dike Swarm, Southern Nevada:
646   Final, Extension-Related Pulse of the Spirit Mountain Batholith. 2005:V13A-01

647 Ghiorso MS, Gualda GAR (2015) An H2O-CO2 mixed fluid saturation model compatible with rhyolite-
648   MELTS. Contributions to Mineralogy and Petrology 169:. https://doi.org/10.1007/s00410-015-
649   1141-8

650 Giordano G, Caricchi L (2022) Determining the State of Activity of Transcrustal Magmatic Systems and
651   Their Volcanoes. Annu Rev Earth Planet Sci 50:231–259. https://doi.org/10.1146/annurev-earth-
652   032320-084733

653 Glazner AF, Coleman DS, Mills RD (2015) The Volcanic-Plutonic Connection. In: Breitkreuz C, Rocchi S
654   (eds) Physical Geology of Shallow Magmatic Systems. Springer International Publishing, Cham,
655   pp 61–82

656 Gualda GAR, Ghiorso MS (2014) Phase-equilibrium geobarometers for silicic rocks based on rhyolite-
657   MELTS. Part 1: Principles, procedures, and evaluation of the method. Contributions to Mineralogy
658   and Petrology 168:. https://doi.org/10.1007/s00410-014-1033-3

659 Gualda GAR, Ghiorso MS (2013a) The Bishop Tuff giant magma body: an alternative to the Standard
660   Model. Contributions to Mineralogy and Petrology 166:755–775. https://doi.org/10.1007/s00410-
661   013-0901-6

662 Gualda GAR, Ghiorso MS (2013b) Low-Pressure Origin of High-Silica Rhyolites and Granites. Journal of
663   Geology 121:537–545. https://doi.org/10.1086/671395

664 Gualda GAR, Ghiorso MS (2015) MELTS_Excel: A Microsoft Excel-based MELTS interface for research and
665   teaching of magma properties and evolution. Geochemistry Geophysics Geosystems 16:315–324.
666   https://doi.org/10.1002/2014GC005545

667 Gualda GAR, Ghiorso MS, Hurst AA, et al (2022) A complex patchwork of magma bodies that fed the
668   Bishop Tuff supereruption (Long Valley Caldera, CA, United States): Evidence from matrix glass
669   major and trace-element compositions. Front Earth Sci 10:798387.
670   https://doi.org/10.3389/feart.2022.798387

671 Gualda GAR, Ghiorso MS, Lemons RV, Carley TL (2012) Rhyolite-MELTS: A modified calibration of MELTS
672   optimized for silica-rich, fluid-bearing magmatic systems. Journal of Petrology 53:875–890.
673   https://doi.org/10.1093/petrology/egr080

674 Gualda GAR, Gravley DM, Deering CD, Ghiorso MS (2019) Magma extraction pressures and the
675   architecture of volcanic plumbing systems. Earth and Planetary Science Letters 522:118–124.
676   https://doi.org/10.1016/j.epsl.2019.06.020

677 Haapala I, Rämö OT, Frindt S (2005) Comparison of Proterozoic and Phanerozoic rift-related basaltic-
678   granitic magmatism. Lithos 80:1–32. https://doi.org/10.1016/j.lithos.2004.04.057

679 Harper BE, Miller CF, Koteas GC, et al (2004) Granites, dynamic magma chamber processes and pluton
680   construction: the Aztec Wash pluton, Eldorado Mountains, Nevada, USA. Transactions of the
681   Royal Society of Edinburgh-Earth Sciences 95:277–295

682 Hildreth W (2004) Volcanological perspectives on Long Valley, Mammoth Mountain, and Mono Craters:
683   Several contiguous but discrete systems. Journal of Volcanology and Geothermal Research
684   136:169–198. https://doi.org/10.1016/j.volgrores.2004.05.019

685 Hinz N, Faulds J, Ramelli A, Green H (2012) Preliminary geologic map of the Ireteba Peaks quadrangle,
686   Clark County, Nevada. Nevada Bureau of Mines and Geology Open-File Report 2012-09

687 Hodge K, Miller C, Miller J, Faulds J (2006) Dike emplacement at the Searchlight, NV, Volcano-Plutonic
688   Complex. In: 102nd Annual Meeting of the Cordilleran Section, GSA, 81st Annual Meeting of the
689   Pacific Section, AAPG, and the Western Regional Meeting of the Alaska Section, SPE

690 Hopson C, Gans P, Baer E, et al (1994) Spirit Mountain pluton, southern Nevada: A progress report. In:
691   Geological Society of America Abstracts with Programs. p 60

692 Howard KA, John BE, Davis GA, et al (1994) A guide to Miocene extension and magmatism in the lower
693   Colorado River region, Nevada, Arizona, and California. U.S. Geological Survey

694 Huber C, Townsend M, Degruyter W, Bachmann O (2019) Optimal depth of subvolcanic magma chamber
695   growth controlled by volatiles and crust rheology. Nat Geosci 12:762–768.
696   https://doi.org/10.1038/s41561-019-0415-6

697 Keller CB, Schoene B, Barboni M, et al (2015) Volcanic–plutonic parity and the differentiation of the
698   continental crust. Nature 523:301–307. https://doi.org/10.1038/nature14584

699 Koteas GC (2005) Documenting the architecture of a stratified, multiply recharged intrusion / by George
700   Christopher Koteas. Thesis M.S. in Geology--Vanderbilt University, May 2005.

701 Lang NP, Walker BJ, Claiborne LL, et al (2008) The Spirit Mountain batholith and Secret Pass Canyon
702   volcanic center: A cross-sectional view of the magmatic architecture of the uppermost crust of an
703   extensional terrain, Colorado River, Nevada-Arizona. In: GSA Field Guide 11: Field Guide to
704   Plutons, Volcanoes, Faults, Reefs, Dinosaurs, and Possible Glaciation in Selected Areas of Arizona,
705   California, and Nevada. Geological Society of America, pp 187–214

706 Lee C-TA, Morton DM (2015) High silica granites: Terminal porosity and crystal settling in shallow magma
707   chambers. Earth and Planetary Science Letters 409:23–31.
708   https://doi.org/10.1016/j.epsl.2014.10.040

709 Leigh MJ, Miller JS, Blackburn T, et al (2018) Timescale for the construction of Aztec Wash Pluton,
710   Southern Nevada. In: Geological Society of America Abstracts with Programs. p 321662

711 Lowery Claiborne L, Miller CF, Walker BA, et al (2006) Tracking magmatic processes through Zr/Hf ratios
712   in rocks and Hf and Ti zoning in zircons: An example from the Spirit Mountain batholith, Nevada.
713   Mineral mag 70:517–543. https://doi.org/10.1180/0026461067050348

714 Magee C, Stevenson CTE, Ebmeier SK, et al (2018) Magma Plumbing Systems: A Geophysical
715   Perspective. Journal of Petrology 59:1217–1251. https://doi.org/10.1093/petrology/egy064

716 Miller CF, Furbish DJ, Walker BA, et al (2011) Growth of plutons by incremental emplacement of sheets in
717   crystal-rich host: Evidence from Miocene intrusions of the Colorado River region, Nevada, USA.
718   Tectonophysics 500:65–77. https://doi.org/10.1016/j.tecto.2009.07.011

719 Miller CF, Miller JS (2002) Contrasting stratified plutons exposed in tilt blocks, Eldorado Mountains,
720   Colorado River Rift, NV, USA. Lithos 61:209–224

721 Pamukcu AS, Gualda GAR, Ghiorso MS, et al (2015) Phase-equilibrium geobarometers for silicic rocks
722   based on rhyolite-MELTS-Part 3: Application to the Peach Spring Tuff (Arizona-California-Nevada,
723   USA). Contributions To Mineralogy and Petrology 169:. https://doi.org/10.1007/s00410-015-
724   1122-y

725 Pamukcu AS, Gualda GAR, Gravley DM (2021) Rhyolite-MELTS and the storage and extraction of large-
726   volume crystal-poor rhyolitic melts at the Taupō Volcanic Center: a reply to Wilson et al. (2021).
727   Contrib Mineral Petrol 176:82. https://doi.org/10.1007/s00410-021-01840-2

728 Patrick DW, Miller CF (1998) Processes in a Composite, Recharging Magma Chamber: Evidence from
729   Magmatic Structures in the Aztec Wash Pluton, Nevada. In: Igneous Petrology. CRC Press

730 Pitcher BW, Gualda GAR, Hasegawa T (2021) Repetitive Duality of Rhyolite Compositions, Timescales,
731   and Storage and Extraction Conditions for Pleistocene Caldera-forming Eruptions, Hokkaido,
732   Japan. Journal of Petrology 62:egaa106. https://doi.org/10.1093/petrology/egaa106

733 Samperton KM, Schoene B, Cottle JM, et al (2015) Magma emplacement, differentiation and cooling in
734   the middle crust: Integrated zircon geochronological–geochemical constraints from the Bergell
735   Intrusion, Central Alps. Chemical Geology 417:322–340.
736   https://doi.org/10.1016/j.chemgeo.2015.10.024

737 Sawyer EW, Cesare B, Brown M (2011) When the Continental Crust Melts. Elements 7:229–234.
738   https://doi.org/10.2113/gselements.7.4.229

739 Schaltegger U, Nowak A, Ulianov A, et al (2019) Zircon Petrochronology and 40Ar/39Ar
740   Thermochronology of the Adamello Intrusive Suite, N. Italy: Monitoring the Growth and Decay of
741   an Incrementally Assembled Magmatic System. Journal of Petrology 60:701–722.
742   https://doi.org/10.1093/petrology/egz010

743 Smithies SL, Harmon LJ, Allen SM, et al (2023) Following magma: The pathway of silicic magmas from
744   extraction to storage during an ignimbrite flare-up, Taupō Volcanic Zone, New Zealand. Earth and
745   Planetary Science Letters 607:118053. https://doi.org/10.1016/j.epsl.2023.118053

746 Tramontano S, Gualda GAR, Ghiorso MS (2017) Internal triggering of volcanic eruptions: tracking
747   overpressure regimes for giant magma bodies. Earth and Planetary Science Letters 472:142–151.
748   https://doi.org/10.1016/j.epsl.2017.05.014

749 Volborth A (1973) Geology of the granite complex of the Eldorado, Newberry, and northern Dead
750   Mountains, Clark County, Nevada. Mackay School of Mines, University of Nevada, Reno

751 Walker BA, Miller CF, Claiborne LL, et al (2007) Geology and geochronology of the Spirit Mountain
752   batholith, southern Nevada: Implications for timescales and physical processes of batholith
753   construction. Journal of Volcanology and Geothermal Research 167:239–262.
754   https://doi.org/10.1016/j.jvolgeores.2006.12.008

755 Wallrich BM, Miller CF, Gualda GAR, et al (2023) Volcano-pluton connection: Perspectives on material and
756   process linkages, Searchlight pluton and Highland Range volcanic sequence, Nevada, USA. Earth-
757   Science Reviews 238:104361. https://doi.org/10.1016/j.earscirev.2023.104361

758 Wiebe RA (1994) Silicic Magma Chambers as Traps for Basaltic Magmas: The Cadillac Mountain Intrusive
759   Complex, Mount Desert Island, Maine. The Journal of Geology 102:423–437.
760   https://doi.org/10.1086/629684

761 Wones DR (1989) Significance of the assemblage titanite+magnetite+quartz in granitic rocks*. American
762   Mineralogist 74:744–749

763

764

765 **FIGURE CAPTIONS**

766 Figure 1. Schematic map showing the distribution of Miocene plutons and associated volcanic sequences

767 in the Colorado River Extensional Corridor (CREC) in southern Nevada. The location of the Aztec Wash

768 Pluton, the Spirit Mountain Batholith, the Searchlight Pluton, and the Highland Range Volcanic Sequence

769 are highlighted.

770 Figure 2. Schematic maps of the Aztec Wash Pluton. (Top) Google Earth image showing the distribution

771 of key units in the pluton – perspective chosen is looking East, toward the pluton roof. (Bottom)

772 Schematic geological map, modified from Koteas (2005); East (roof) is at the top, matching orientation of

773 Google Earth image. Dashed rectangle in bottom panel shows approximate location of Google Earth

774 image shown at top.

775 Figure 3. Schematic maps of the Spirit Mountain Batholith. (Top) Google Earth image showing the

776 distribution of key units in the pluton – perspective chosen is looking West, toward the pluton roof.

777 (Bottom) Schematic geological map, modified from Walker et al. (2007); West (roof) is at the top,

778 matching orientation of Google Earth image.

779 Figure 4. Schematic maps of the Searchlight Pluton and the Highland Range Volcanic Sequence. (Top)

780 Google Earth image showing the distribution of key units in the pluton and the location of the Highland

781 Range Volcanic Sequence. (Bottom) Schematic cross section of the Searchlight Pluton and the Highland

782 Range Volcanic Sequence, modified from Wallrich *et al*. (2023).

783 Figure 5. Schematic diagram highlighting the difference between extraction and pre-eruptive storage

784 pressures. Extraction pressures record the pressures at which magma mushes are present, from which

785 magmas are extracted and mobilized to shallower levels. Pre-eruptive storage pressures record pressures

786 at which melt-dominated magmas are stored and crystallize prior to eruption to the surface. See text for

787 more details.

31

788   Figure 6. Example pressure calculations using the rhyolite-MELTS geobarometer (Gualda and Ghiorso

789   2014). (a) Example of a calculation that yields a quartz, 2 feldspars, magnetite, and ilmenite (Q2FMI)

790   pressure. (b) Example of a calculation that yields a quartz and 2 feldspars (Q2F) pressure. (c-d) Examples

791   of calculations that do not yield either a Q2FMI or Q2F pressure – in this work, we do not use the

792   resulting two-phase pressures that could be inferred from these calculations. In (a) and (b), the best

793   pressure estimate is indicated by the arrow and the calculated pressure is shown above the arrow.

794   Figure 7. Harker diagrams showing compositional patterns in the units studied here. Blue symbols

795   correspond to rocks from the Aztec Wash Pluton (labelled "AW"); all compositions are whole-rock

796   compositions. Gray symbols correspond to rocks from the Spirit Mountain Batholith ("SM"); all

797   compositions are whole-rock compositions. Green symbols correspond to rocks from the Middle

798   Searchlight Unit ("MSL"); all compositions are whole-rock compositions. Orange symbols correspond to

799   rocks from the Upper Highland Range Volcanic Sequence ("HR"); whole-rock compositions are labelled as

800   "WR", while glass compositions are labelled as "GL". We identify three compositional groups, as indicated

801   at the top of the figure.

802   Figure 8. TiO_2 versus SiO_2 diagram showing the potential genetic relationship between the various facies

803   in the Aztec Wash Pluton (top left), Searchlight Pluton (top right), and Spirit Mountain Batholith (bottom).

804   Compositions with intermediate SiO_2 in the diagram may represent input compositions that continuously

805   fed these systems (indicated as "Input magma?"). Low-SiO_2 compositions may correspond to magma

806   mush (i.e., cumulates; "Cumulates?"). High-SiO_2 compositions may represent melt-dominated magmas

807   extracted from magma mush ("Extracted melts?").

808   Figure 9. Pressure versus SiO_2 diagram showing pressures derived using the rhyolite-MELTS

809   geobarometer. Left diagram shows compositions using symbols as in Figure 7 while right diagram shows

810   compositions using symbols that highlight groups 2, 3a, and 3b for each magmatic system. Note the

811   multi-tiered distribution of pressures from these magmatic systems.

812   Figure 10. Projection of compositions onto the haplogranitic ternary using the projection scheme of

813   Blundy & Cashman (2001). Similar to Figure 9, two diagrams are shown with different sets of symbols.

814   The distribution of compositions relative to the quartz-feldspar cotectic is consistent with the rhyolite-

815   MELTS pressures, lending support to the conclusions drawn in this study.

816   Figure 11. Rank-order diagram (a) and histograms (b-d) showing the vertical distribution of rhyolite-

817   MELTS pressures. Blue symbols correspond to rocks from the Aztec Wash Pluton; gray symbols

818   correspond to rocks from Spirit Mountain Batholith; green symbols correspond to rocks from the Middle

819   Searchlight Unit; orange symbols correspond to rocks from the Upper Highland Range Volcanic Sequence.

820   Extraction pressures are shown as solid symbols, while pre-eruptive storage pressures are shown as

821   stippled symbols. Note the discontinuous distribution of pressures for all three systems (see text for

822   details).

823   Figure 12. Pressure versus SiO_2 diagrams showing the results of isobaric rhyolite-MELTS calculations

824   exploring the differentiation of silica-rich magmas within the middle to shallow crust. Symbols as in Figure

825   9. Vertical lines suggest ascent of magmas to shallower levels, followed by progressive solidification

826   (black horizontal lines) until the quartz-2 feldspars-fluid near-invariant (red triangles) is reached.

827   Fractional crystallization of group 2 compositions explains well the compositions of group 3a magmas, but

828   not the compositions of group 3b magmas. Fractional crystallization of group 3a magmas much better

829   explains the generation of group 3b magmas. This suggests magma differentiation in a step-wise manner

830   through the middle to upper crustal magmatic column.

831   Figure 13. Evolution of crystal contents (% solids) as a function of temperature for isobaric rhyolite-

832   MELTS calculations using group 3a (top) and group 2 (bottom) compositions. Each curve corresponds to

833   a combination of composition and pressure used. Different pressures are illustrated with different shades

834   of cyan (group 3a) and magenta (group 2) and by different symbols. Symbols correspond to – in this

835   order – the conditions of saturation of the first feldspar (labeled feldspar1), the second feldspar

836   (feldspar2), and quartz. All curves show that upon saturation in quartz the system attains a near-invariant

837   behavior, with nearly isothermal solidification, suggesting that the system is thermally buffered after

838   saturation in quartz. This suggests that such magma mushes would allow extraction of melt-dominated

839   melt with nearly constant silica contents.

840   Figure 14. Schematic cross-section representative of the architecture of the Aztec Wash and Middle

841   Searchlight-Upper Highland Range Magmatic Systems. Dotted patterns represent magma mush (i.e.,

842   cumulate); solid colors represent melt (whole-rock) compositions preserved as plutonic rocks; stippled

843   patterns represent melt (glass) compositions preserved in volcanic rocks. Location of magma mush is

844   inferred from extraction pressures, while the location of melt-dominated magma is inferred from pre-

845   eruptive storage pressures. Magenta colors show a mid-crustal mush system, while cyan and yellow

846   colors show shallow-crustal mush systems. The mid-crustal mush system is inferred from extraction

847   pressures, while the shallow-crustal mush systems represent the crustal level exposed by the plutons.

848

849   **TABLES**

850   **Table 1.** Whole-rock compositions.

851

852
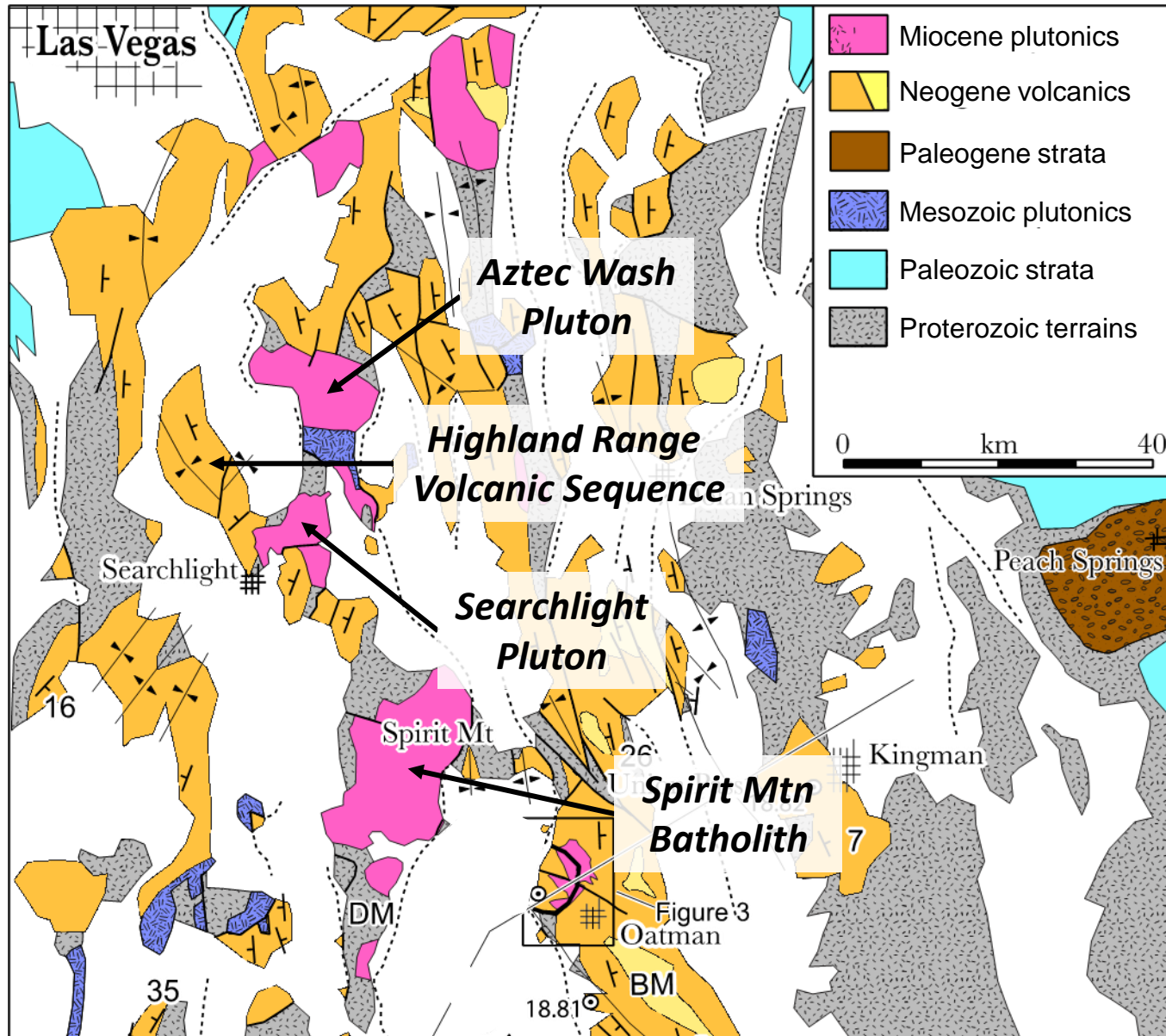
Figure 1
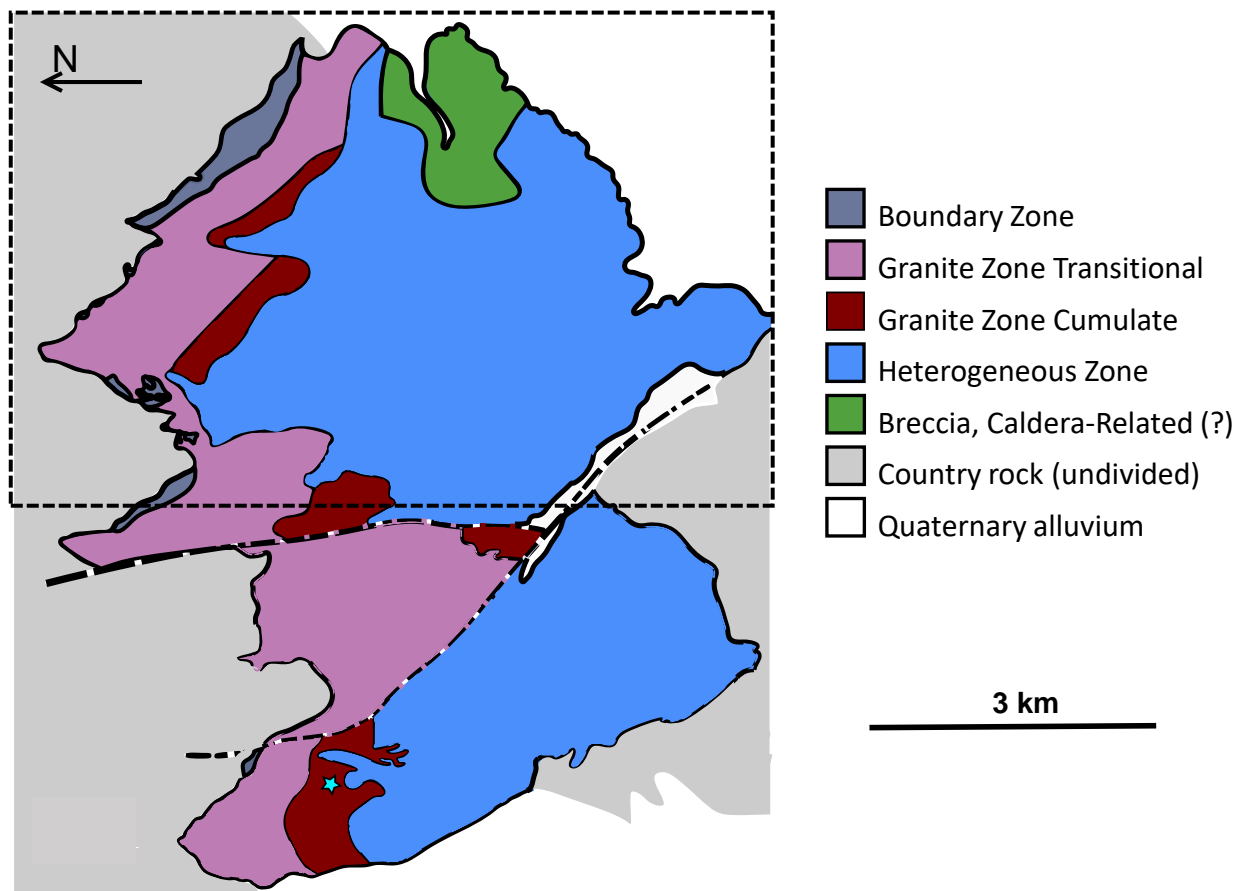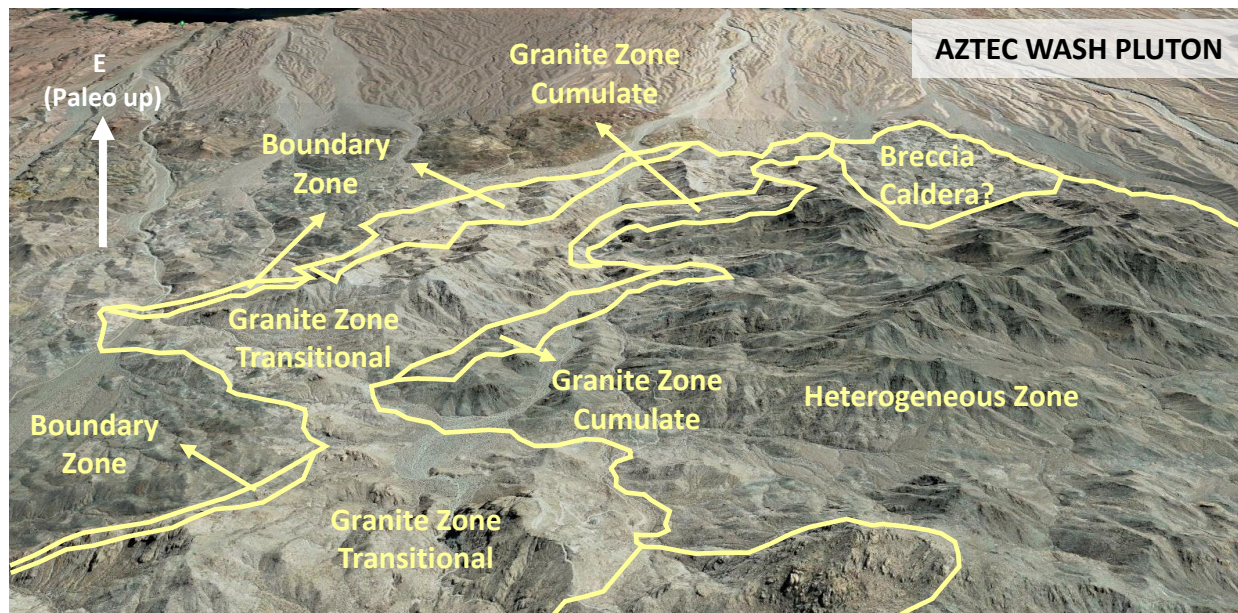
Figure 2
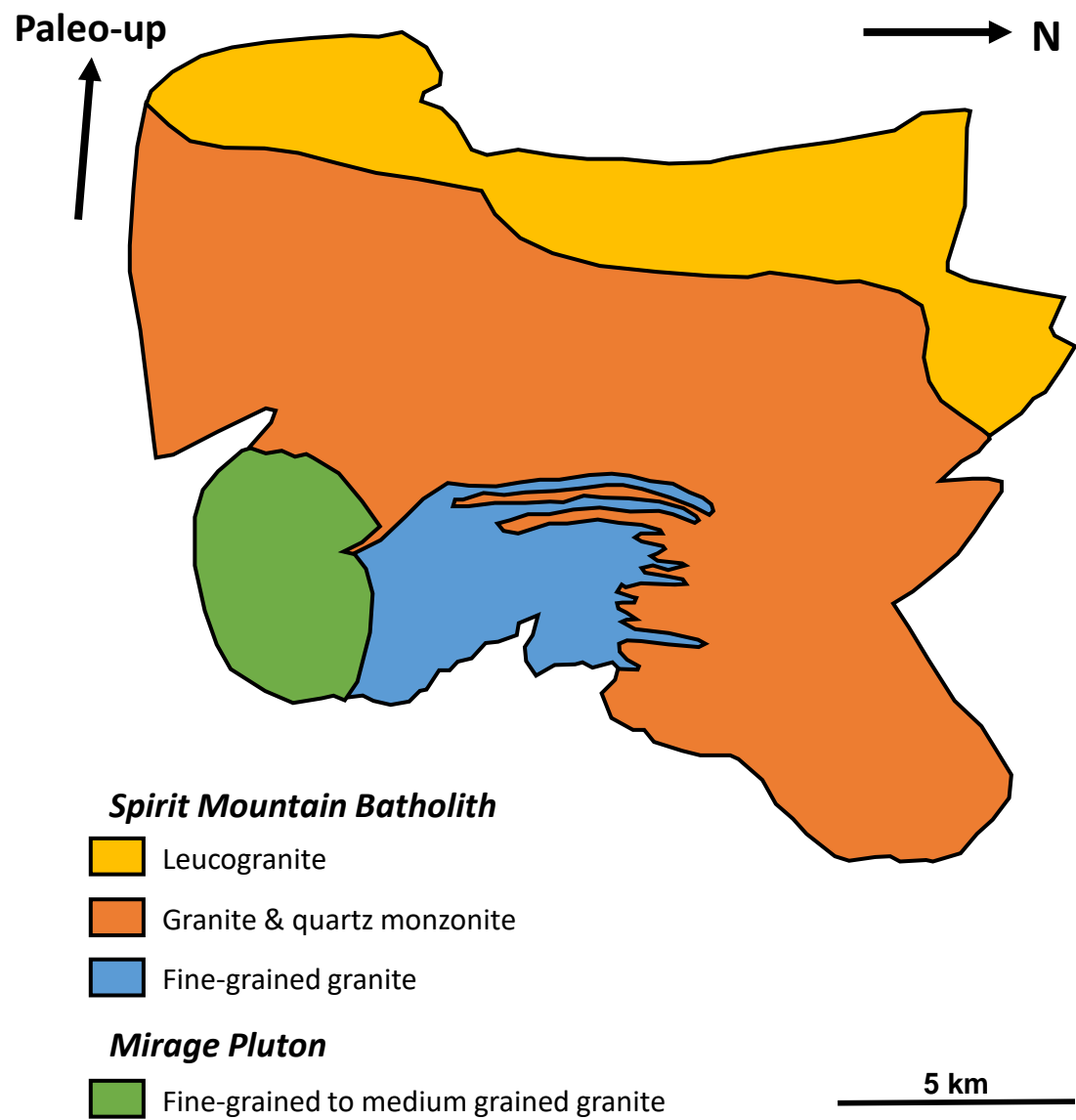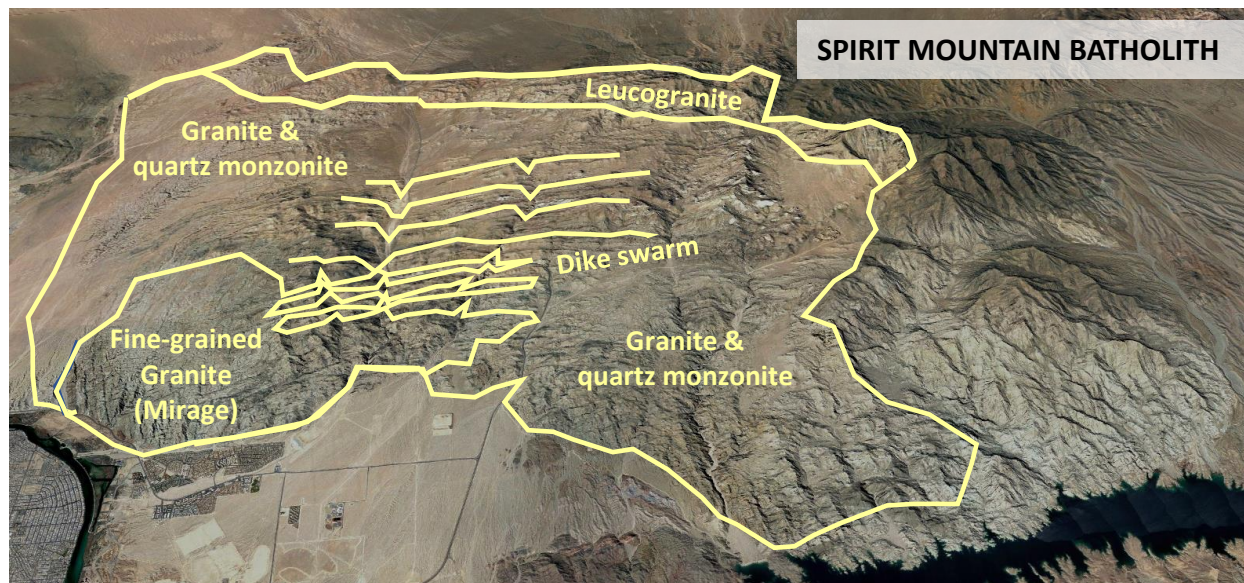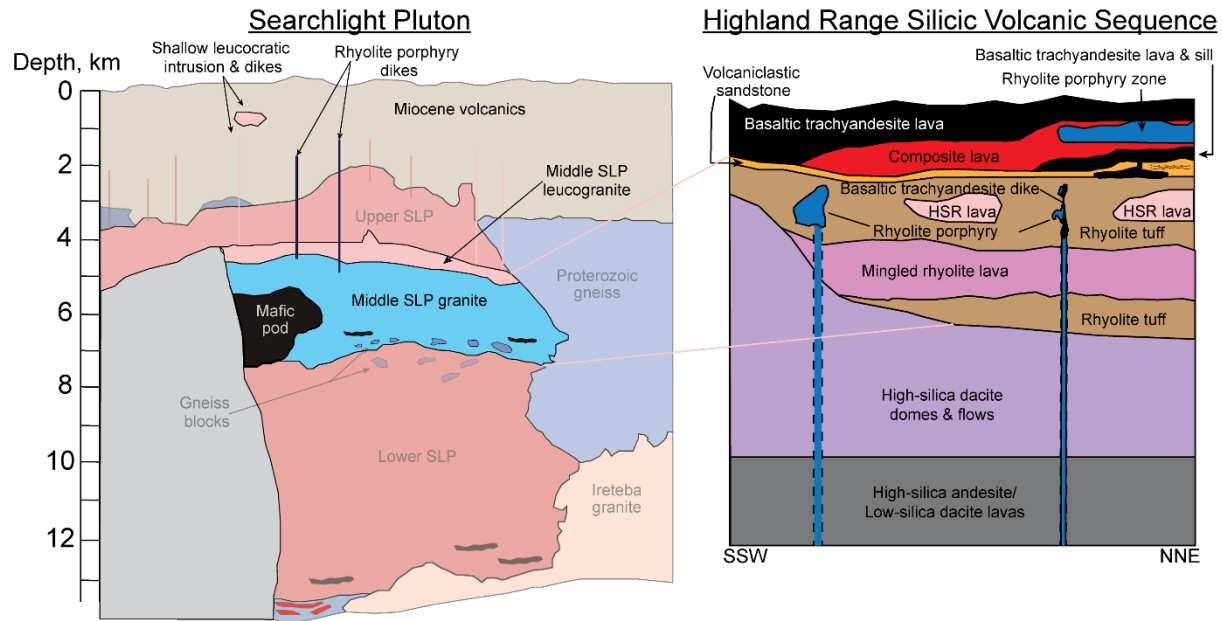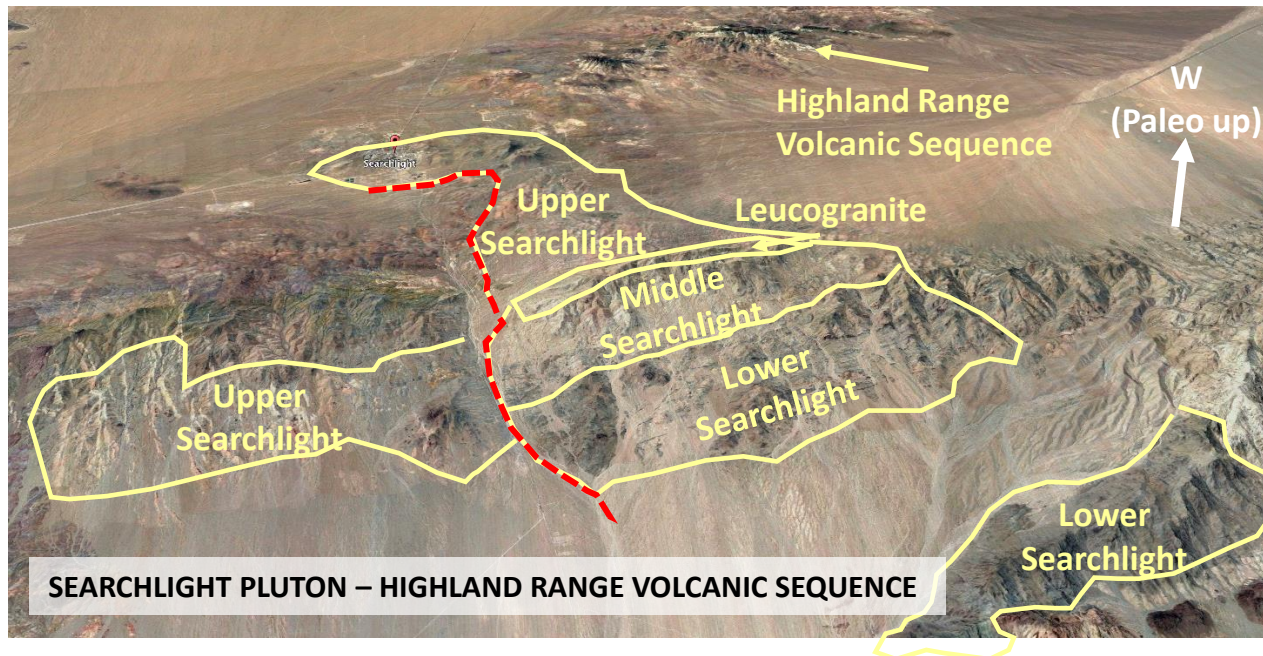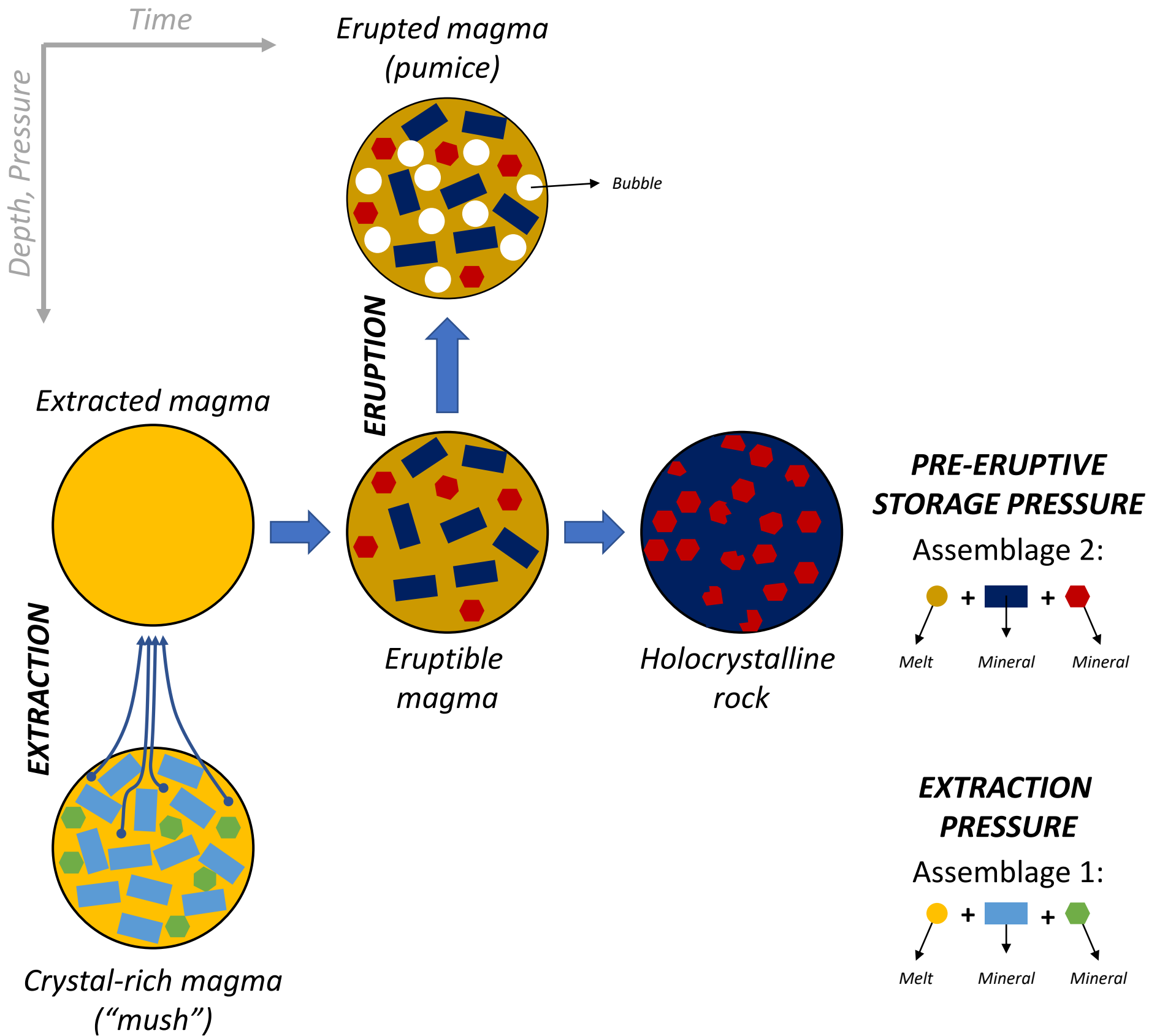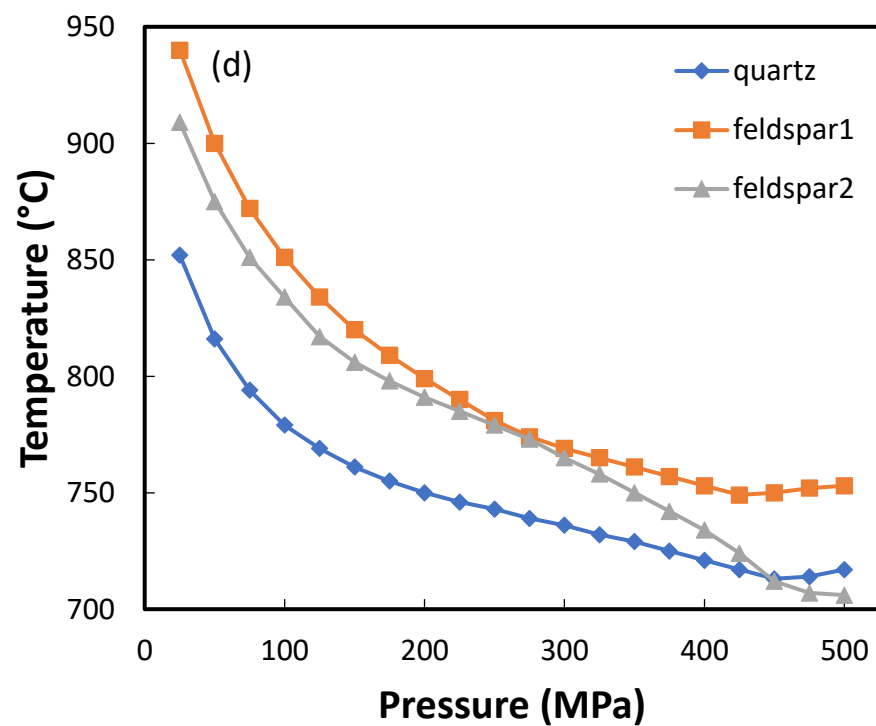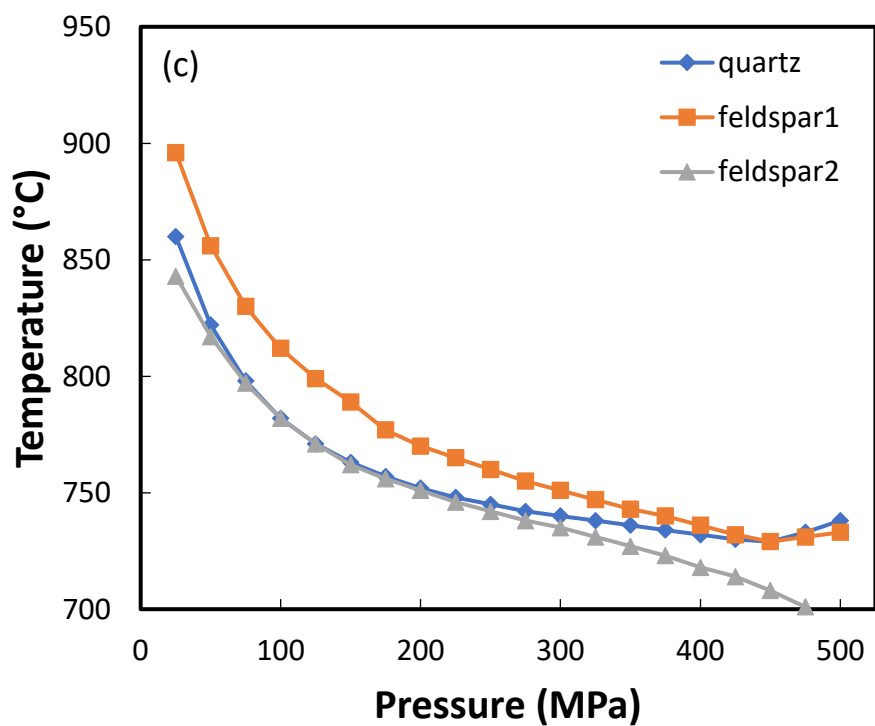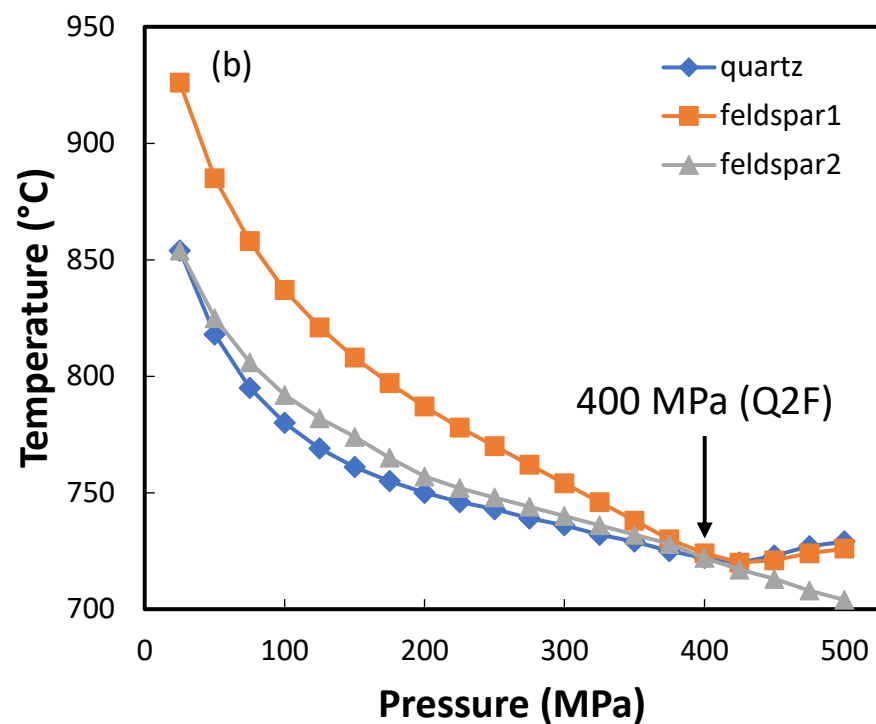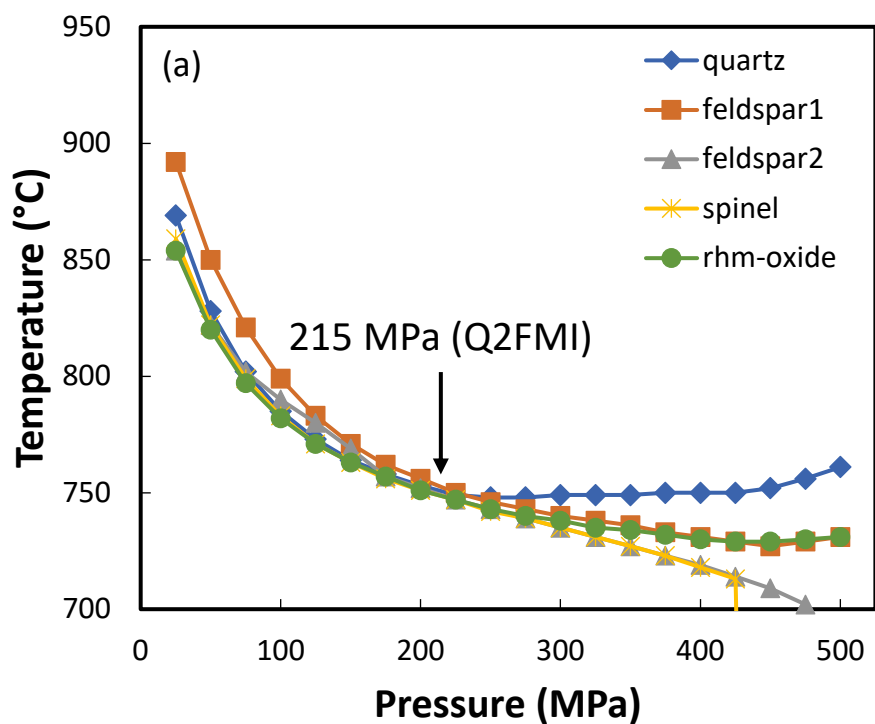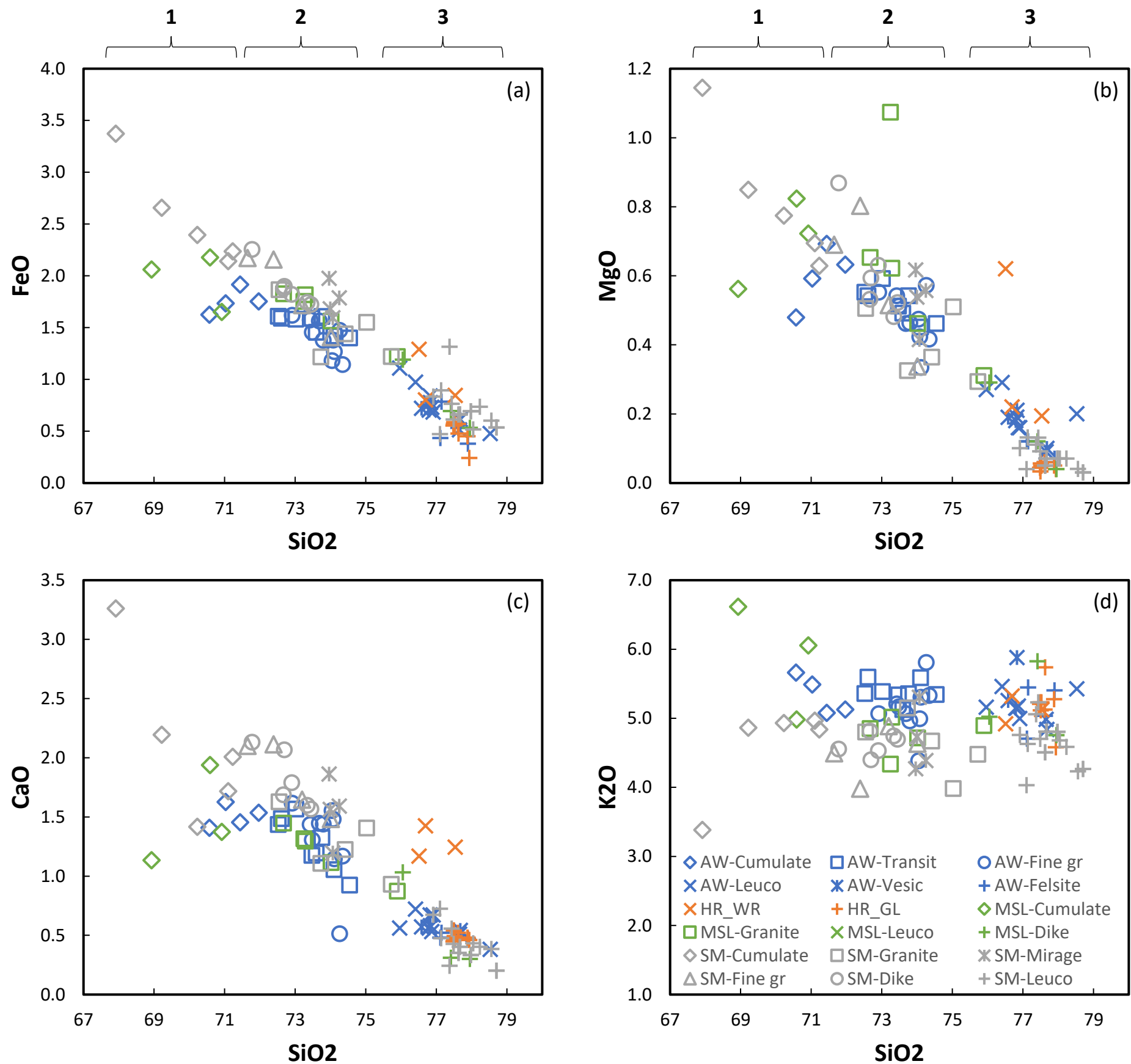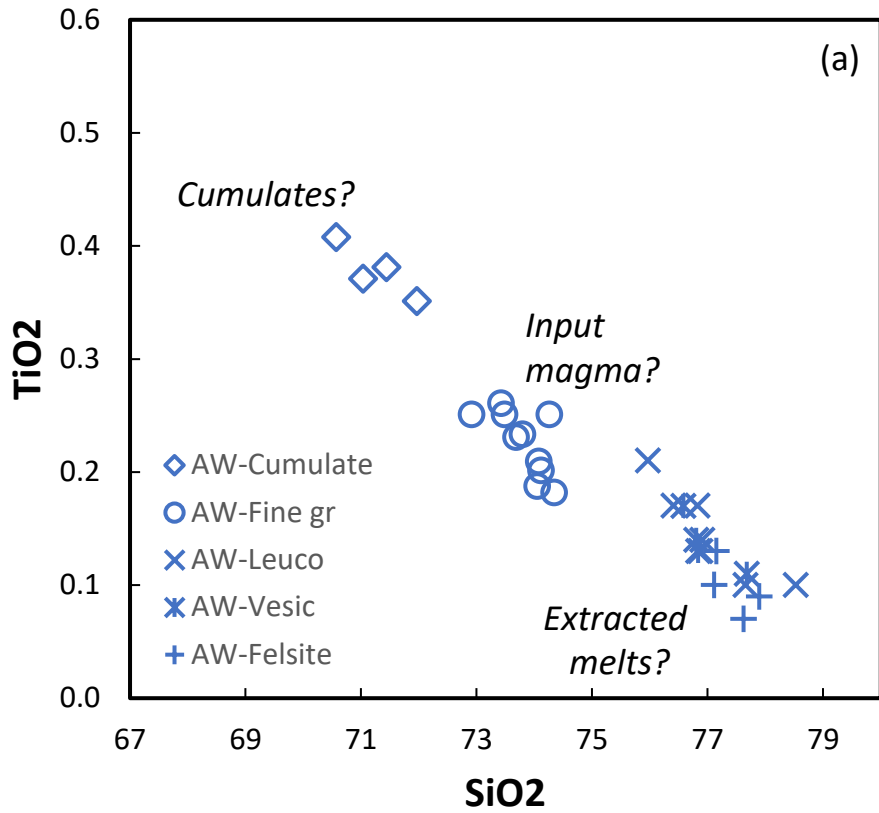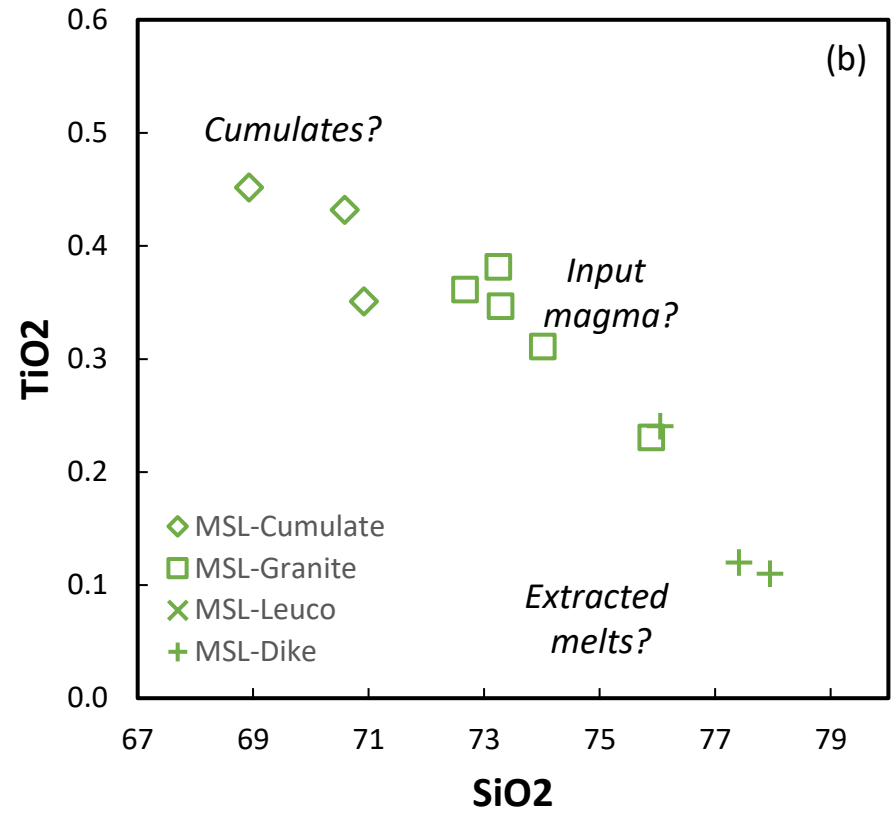
Paleo-up

N

Spirit Mountain Batholith

- Leucogranite
- Granite & quartz monzonite
- Fine-grained granite

Mirage Pluton

- Fine-grained to medium grained granite

5 km

Figure 3

SEARCHLIGHT PLUTON – HIGHLAND RANGE VOLCANIC SEQUENCE
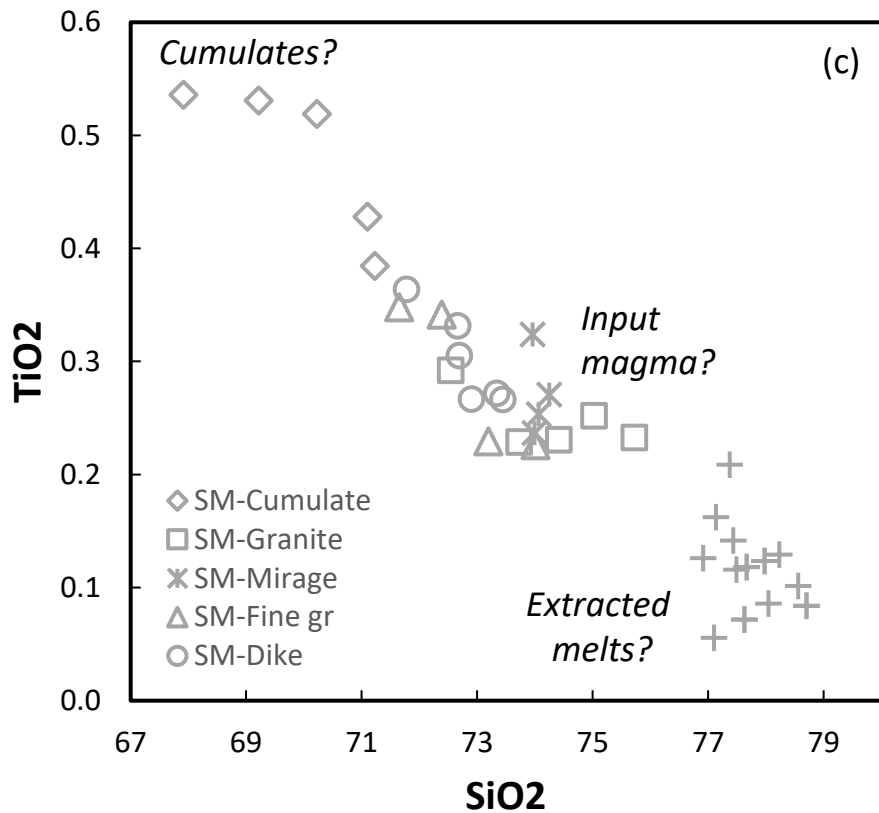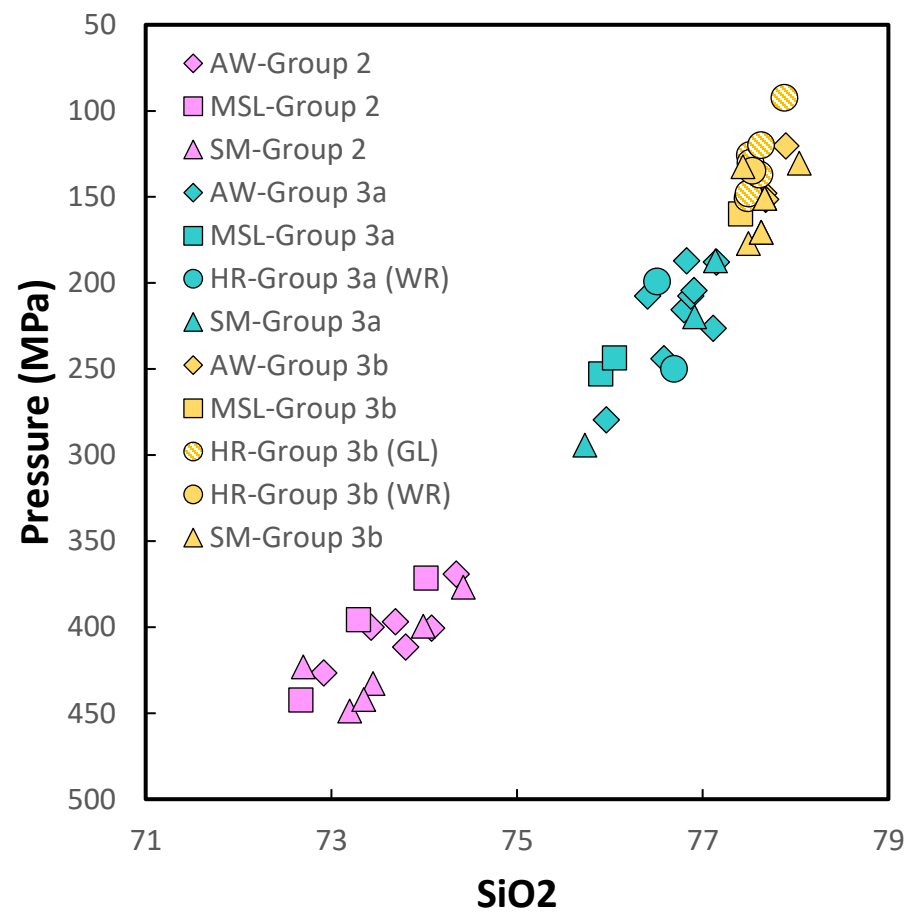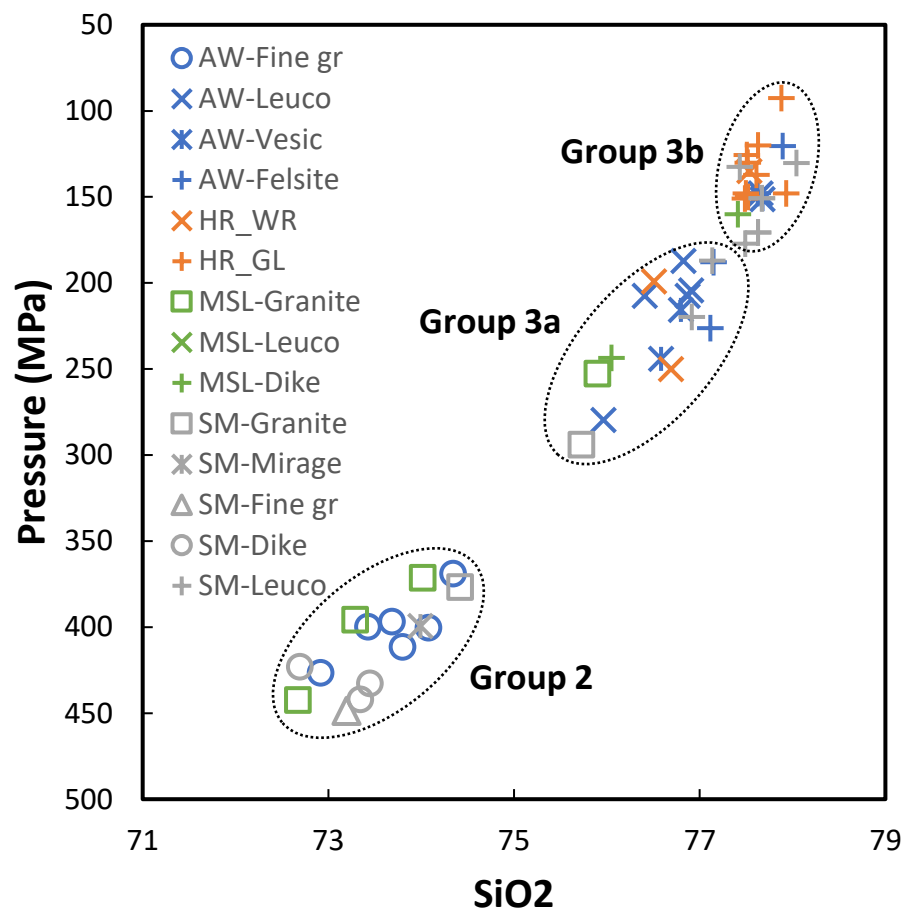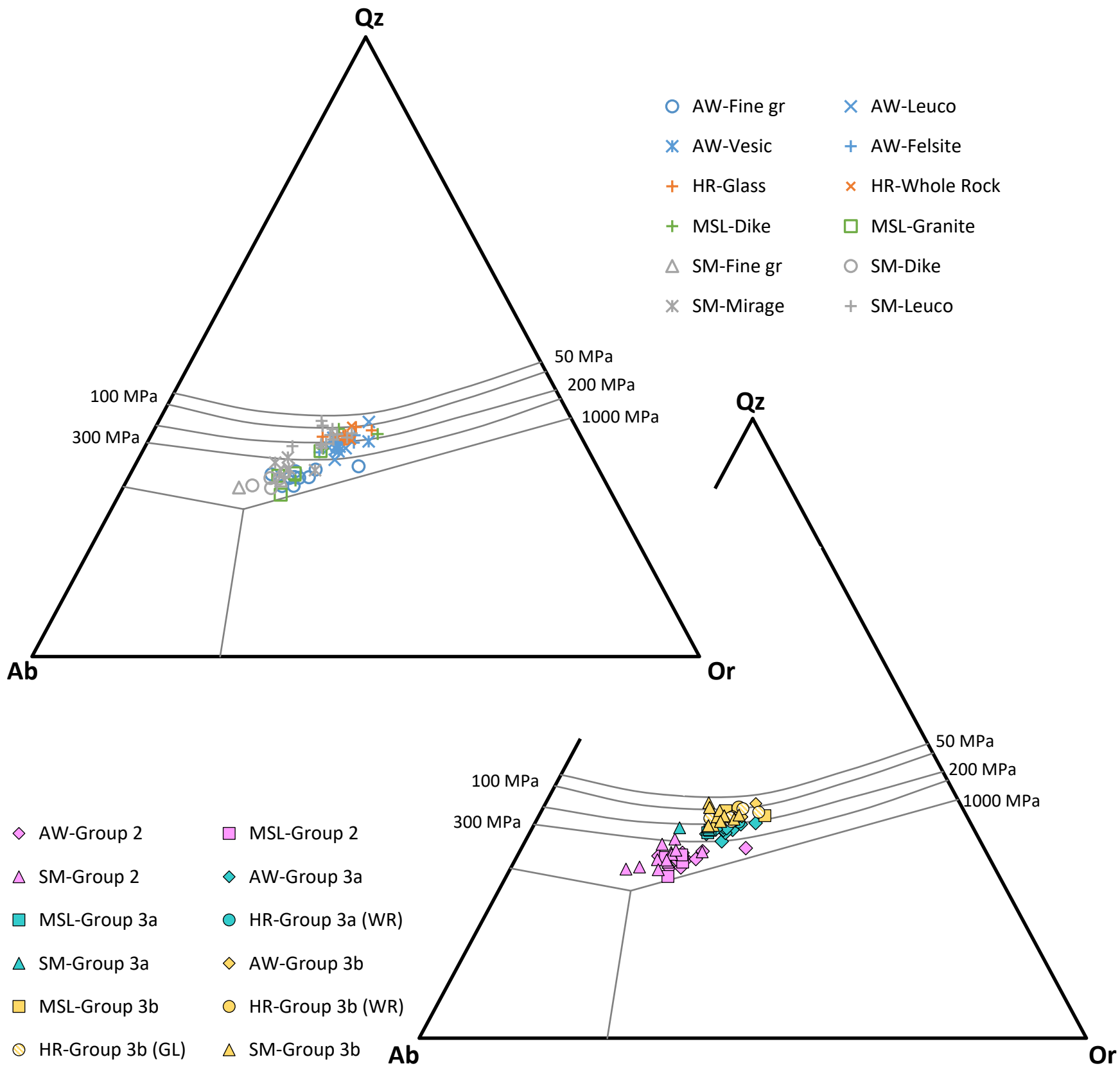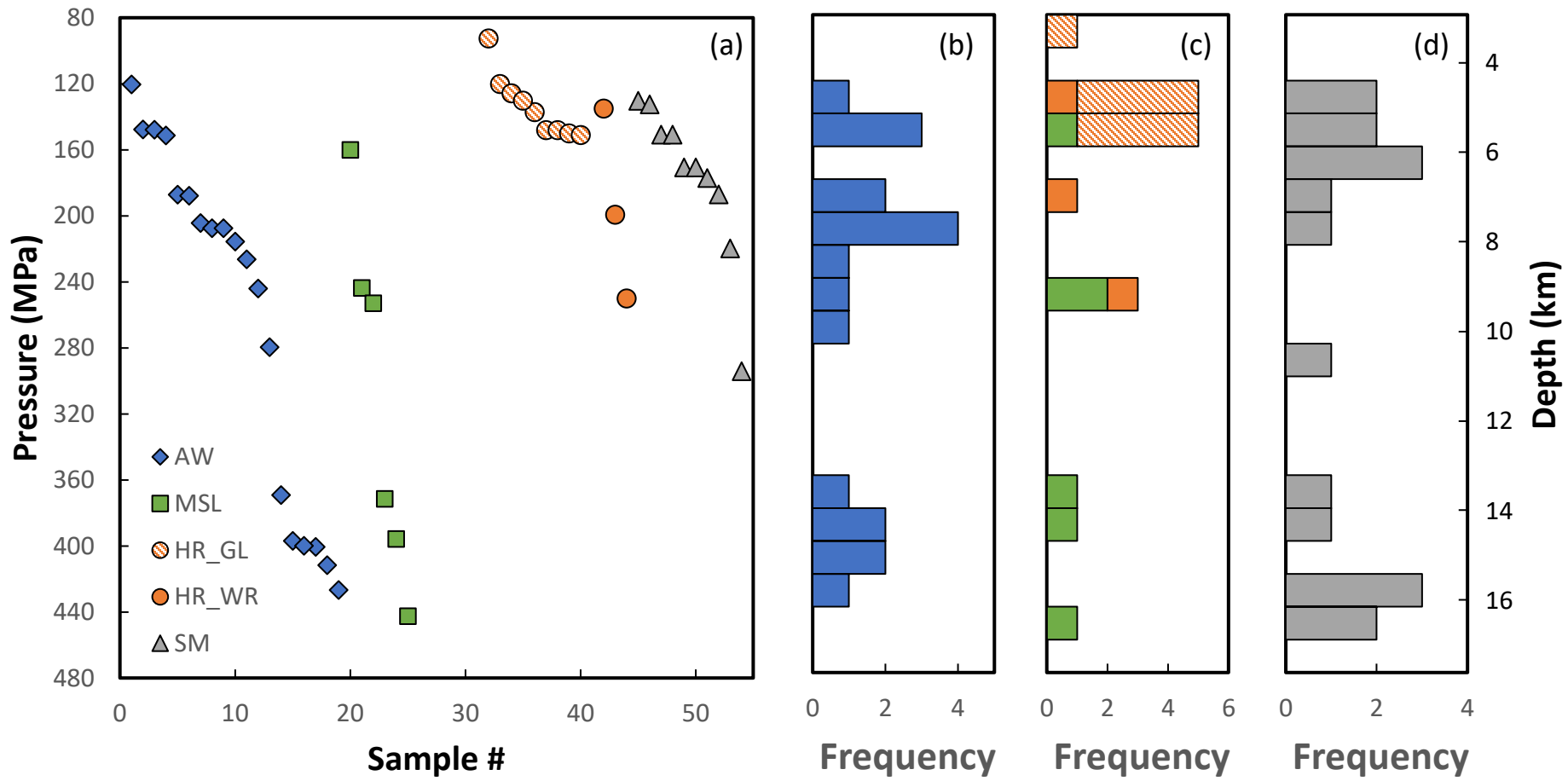
Figure 4

Figure 5

Figure 6

Figure 7

Figure 8

Figure 9

Figure 10

Figure 11

Figure 12

Figure 13

Figure 14
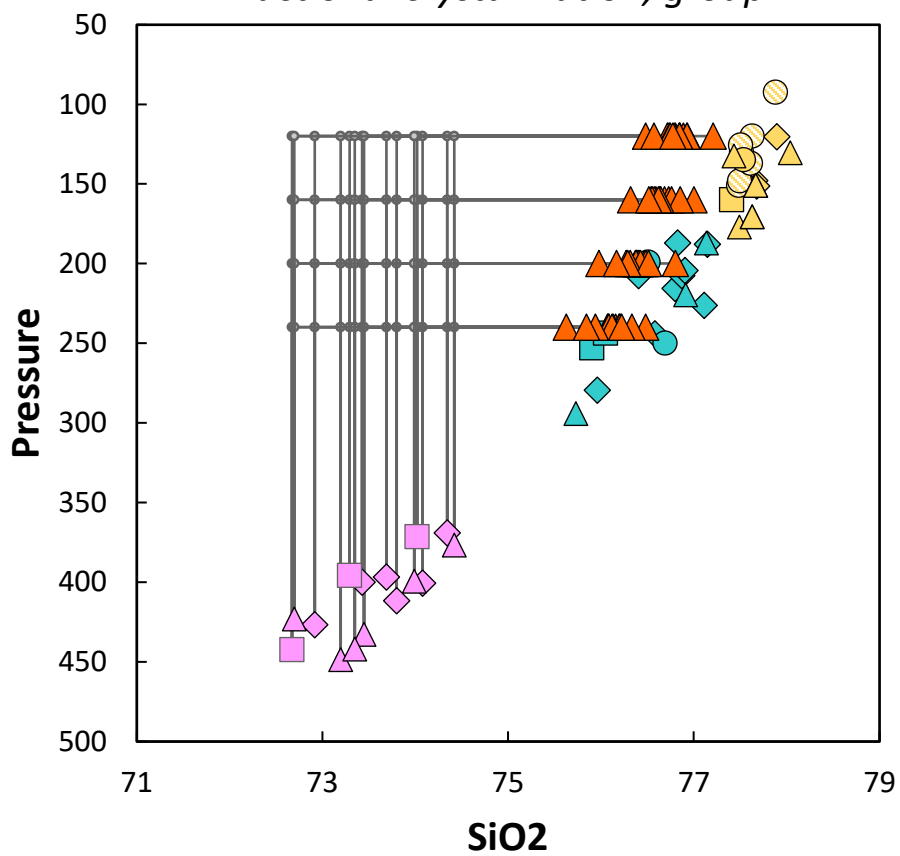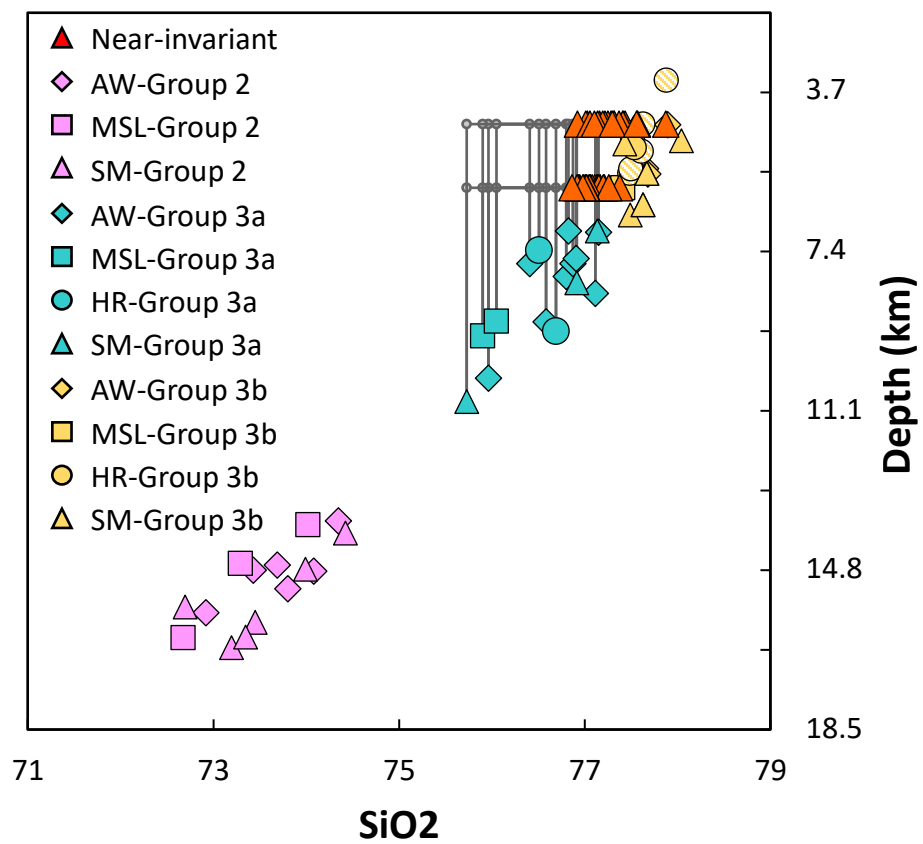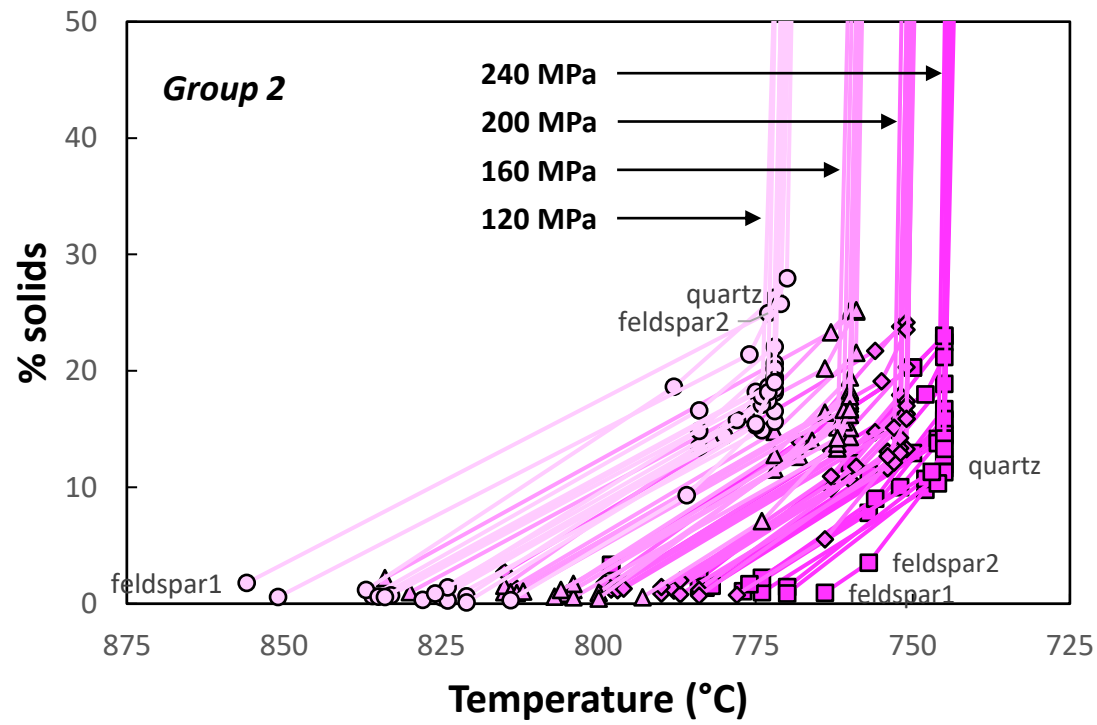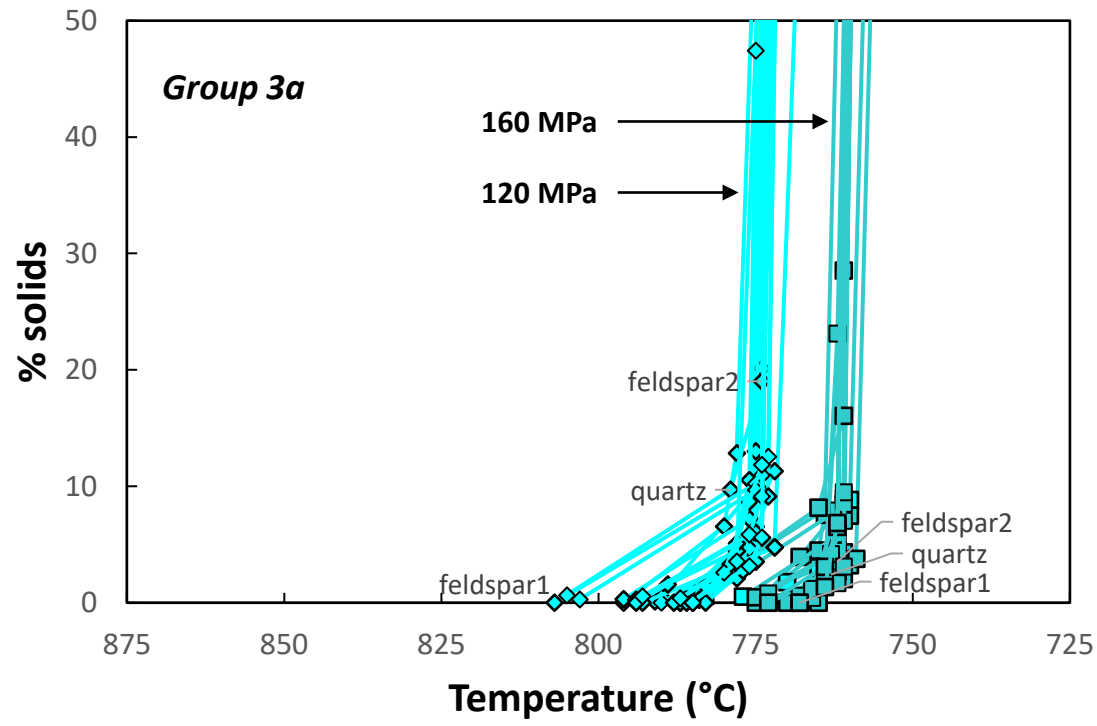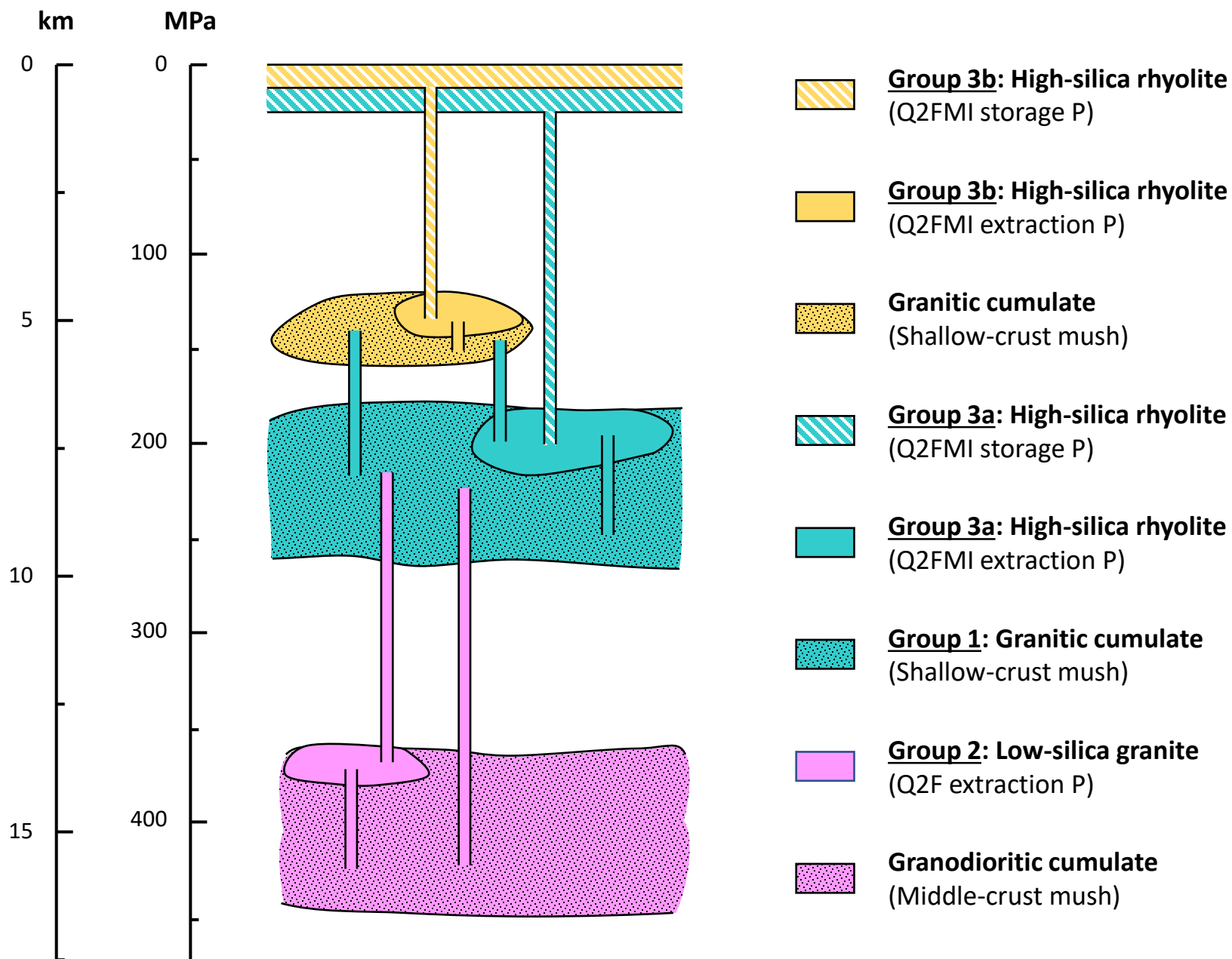
Table 1. Whole-rock and glass compositions.

Sample	Unit	Type	Group	SiO_2	TiO_2	Al_2O_3	FeO	MnO	MgO	CaO	Na_2O	K_2O	P (MPa)	Assemblage
HAW-18-BH	AW	WR	AW-Group 1	71.0	0.37	15.2	1.73	0.03	0.59	1.63	3.96	5.49	-	-
HAW-5-BH	AW	WR	AW-Group 1	72.0	0.35	14.6	1.75	0.04	0.63	1.53	3.99	5.13	-	-
AW29	AW	WR	AW-Group 1	70.6	0.41	15.5	1.62	0.00	0.48	1.41	4.35	5.66	-	-
HAW-2	AW	WR	AW-Group 1	71.4	0.38	15.2	1.91	0.00	0.69	1.45	3.89	5.08	-	-
HAW-84-BH	AW	WR	AW-Group 2	72.9	0.25	14.5	1.62	0.00	0.55	1.61	3.52	5.07	427	Q2F
NAWZ53-BH	AW	WR	AW-Group 2	73.4	0.26	14.2	1.57	0.00	0.54	1.43	3.38	5.20	400	Q2F
AWD10-CM	AW	WR	AW-Group 2	73.5	0.25	14.1	1.45	0.00	0.51	1.30	3.72	5.16	-	-
HAW-1-BH	AW	WR	AW-Group 2	73.7	0.23	14.1	1.56	0.00	0.46	1.44	3.48	5.06	397	Q2F
AW566-CM	AW	WR	AW-Group 2	73.8	0.23	14.1	1.38	0.00	0.46	1.44	3.61	4.96	412	Q2F
NAWZ13-CM	AW	WR	AW-Group 2	74.1	0.19	14.3	1.18	0.00	0.47	1.55	3.84	4.38	-	-
AW550-CM	AW	WR	AW-Group 2	74.1	0.21	14.0	1.38	0.00	0.42	1.48	3.41	4.99	401	Q2F
AW557-CM	AW	WR	AW-Group 2	74.1	0.20	14.0	1.27	0.00	0.33	1.14	3.61	5.30	-	-
HAW-80-BH	AW	WR	AW-Group 2	74.3	0.25	13.8	1.47	0.00	0.57	0.51	3.36	5.81	-	-
AW542-CM	AW	WR	AW-Group 2	74.3	0.18	14.0	1.14	0.00	0.42	1.17	3.40	5.33	369	Q2F
HAW-10-BH	AW	WR	AW-Group 2	73.0	0.30	14.0	1.58	0.04	0.59	1.56	3.54	5.38	-	-
HAW-21-BH	AW	WR	AW-Group 2	72.5	0.32	14.3	1.61	0.03	0.55	1.43	3.86	5.35	-	-
HAW-35-BH	AW	WR	AW-Group 2	72.6	0.32	14.1	1.59	0.04	0.54	1.48	3.69	5.59	-	-
HAW-56-BH	AW	WR	AW-Group 2	73.5	0.32	14.0	1.59	0.03	0.51	1.17	3.61	5.33	-	-
HAW-60-BH	AW	WR	AW-Group 2	73.6	0.29	14.0	1.45	0.04	0.49	1.19	3.82	5.12	-	-
HAW-64-BH	AW	WR	AW-Group 2	74.5	0.28	13.4	1.40	0.04	0.46	0.92	3.59	5.34	-	-
NAW-Z50-BH	AW	WR	AW-Group 2	74.1	0.27	13.7	1.42	0.03	0.45	1.05	3.40	5.58	-	-
NAW-Z52-BH	AW	WR	AW-Group 2	73.8	0.32	13.6	1.61	0.03	0.54	1.32	3.47	5.35	-	-
HAW-47-BH	AW	WR	AW-Group 3a	76.0	0.21	12.8	1.11	0.00	0.27	0.56	3.90	5.16	280	Q2F
AWZ1B-BH	AW	WR	AW-Group 3a	76.4	0.17	12.7	0.97	0.00	0.29	0.72	3.30	5.46	208	Q2FMI
AW75-BH	AW	WR	AW-Group 3a	76.6	0.17	12.8	0.72	0.00	0.19	0.57	3.66	5.26	244	Q2FMI
NAW-Z-26-BH	AW	WR	AW-Group 3a	76.8	0.14	12.8	0.70	0.00	0.18	0.56	3.69	5.15	216	Q2FMI
HAW-26-BH	AW	WR	AW-Group 3a	76.8	0.17	12.6	0.84	0.00	0.19	0.67	3.56	5.15	187	Q2FMI
HAW-83-BH	AW	WR	AW-Group 3a	76.8	0.13	12.6	0.77	0.00	0.21	0.58	3.00	5.88	-	-
HAW-15-BH	AW	WR	AW-Group 3a	76.9	0.13	12.7	0.73	0.00	0.16	0.53	3.65	5.18	207	Q2FMI

Sample	Loc	Type	Group												
HAW-36-BH	AW	WR	AW-Group 3a	76.9	0.14	12.7	0.68	0.00	0.16	0.67	3.72	5.00		204	Q2FMI
EW20B-BH	AW	WR	AW-Group 3a	77.1	0.10	12.8	0.43	0.00	0.12	0.48	4.22	4.71		226	Q2FMI
HAW-16-BH	AW	WR	AW-Group 3a	77.1	0.13	12.4	0.78	0.00	0.12	0.52	3.44	5.45		188	Q2FMI
HAW-3-BH	AW	WR	AW-Group 3b	77.6	0.07	12.5	0.53	0.00	0.06	0.50	3.68	5.04		148	Q2FMI
HAW-59-BH	AW	WR	AW-Group 3b	77.7	0.10	12.5	0.51	0.00	0.09	0.51	3.69	4.98		148	Q2FMI
HAW-38-BH	AW	WR	AW-Group 3b	77.7	0.11	12.3	0.61	0.00	0.10	0.54	3.81	4.84		151	Q2FMI
HAW-20-BH	AW	WR	AW-Group 3b	77.9	0.09	12.3	0.38	0.00	0.07	0.47	3.40	5.40		120	Q2FMI
HAW-55-BH	AW	WR	AW-Group 3b	78.5	0.10	11.7	0.48	0.00	0.20	0.38	3.20	5.43	-		-
HRE8-EK	HR	WR	HR-Group 3a (WR)	76.5	0.21	12.1	1.29	0.00	0.62	1.17	3.21	4.92		199	Q2F
HRL41A-CM	HR	WR	HR-Group 3a (WR)	76.7	0.11	12.2	0.80	0.00	0.22	1.42	3.25	5.32		250	Q2FMI
HRW13-BW	HR	GL	HR-Group 3b (GL)	77.9	0.08	12.5	0.24	0.00	0.04	0.46	4.01	4.58		148	Q2F
HRE6-EK	HR	WR	HR-Group 3b (WR)	77.5	0.14	11.8	0.84	0.00	0.19	1.25	3.11	5.12		135	Q2F
HRL16_TS-Pum1	HR	GL	HR-Group 3b (GL)	77.5	0.08	12.5	0.56	0.00	0.05	0.48	3.57	5.23		150	Q2FMI
HRL16_TS-Pum2	HR	GL	HR-Group 3b (GL)	77.5	0.11	12.5	0.55	0.00	0.04	0.45	3.58	5.21		151	Q2FMI
HRL16_TS-Pum5-A	HR	GL	HR-Group 3b (GL)	77.5	0.13	12.4	0.59	0.00	0.06	0.46	3.55	5.11		126	Q2FMI
HRL16_TS-Pum6-A	HR	GL	HR-Group 3b (GL)	77.5	0.09	12.5	0.56	0.00	0.05	0.49	3.49	5.22		130	Q2FMI
HRL16-LC	HR	GL	HR-Group 3b (GL)	77.6	0.11	12.5	0.48	0.00	0.05	0.46	3.03	5.74		120	Q2F
HRL21-LC	HR	GL	HR-Group 3b (GL)	77.9	0.12	12.5	0.45	0.00	0.05	0.48	3.27	5.27		93	Q2F
HRL16	HR	GL	HR-Group 3b (GL)	77.5	0.08	12.4	0.57	0.00	0.03	0.54	3.53	5.23		148	Q2F
HRL21	HR	GL	HR-Group 3b (GL)	77.6	0.11	12.5	0.57	0.00	0.06	0.52	3.53	5.13		137	Q2FMI
SL1-CB	MSL	WR	MSL-Group 1	68.9	0.45	16.0	2.06	0.00	0.56	1.13	4.27	6.61	-		-
GG7-CB	MSL	WR	MSL-Group 1	70.6	0.43	15.3	2.18	0.00	0.82	1.94	3.77	4.98	-		-
SL23-CB	MSL	WR	MSL-Group 1	70.9	0.35	15.1	1.65	0.00	0.72	1.37	3.78	6.06	-		-
92140-CB	MSL	WR	MSL-Group 2	72.7	0.36	14.2	1.82	0.00	0.65	1.45	4.04	4.85		442	Q2F
SL77-CB	MSL	WR	MSL-Group 2	73.3	0.38	14.0	1.75	0.00	1.07	1.31	3.87	4.33	-		-
SL200Z-CM	MSL	WR	MSL-Group 2	73.3	0.35	14.0	1.82	0.00	0.62	1.29	3.63	5.01		396	Q2F
SL33-CB	MSL	WR	MSL-Group 2	74.0	0.31	13.9	1.56	0.00	0.46	1.11	3.87	4.71		371	Q2F
SL48-CB	MSL	WR	MSL-Group 3a	75.9	0.23	13.0	1.22	0.00	0.31	0.87	3.58	4.89		253	Q2F
SL76-CB	MSL	WR	MSL-Group 3a	76.0	0.24	12.8	1.19	0.00	0.29	1.03	3.34	5.02		244	Q2F
SL43-CM	MSL	WR	MSL-Group 3b	77.4	0.12	12.4	0.69	0.00	0.12	0.31	3.12	5.82		160	Q2FMI
SL55-CB	MSL	WR	MSL-Group 3b	77.9	0.11	12.5	0.53	0.00	0.04	0.30	3.80	4.75	-		-
BD16	SM	WR	SM-Group 1	71.8	0.36	14.4	2.25	0.00	0.87	2.13	3.63	4.55		429	Q2F

Sample			Group												
BW62	SM	WR	SM-Group 1	71.6	0.35	14.9	2.17	0.00	0.69	2.10	3.66	4.49	-		-
BW33	SM	WR	SM-Group 1	71.2	0.38	15.1	2.24	0.00	0.63	2.01	3.61	4.84	-		-
BC101Z	SM	WR	SM-Group 1	71.1	0.43	14.8	2.14	0.06	0.69	1.72	4.08	4.96	-		-
101Z	SM	WR	SM-Group 1	70.2	0.52	15.2	2.39	0.06	0.77	1.42	4.44	4.93	-		-
BW49/DSCG	SM	WR	SM-Group 1	69.2	0.53	15.6	2.66	0.06	0.85	2.19	4.02	4.86	-		-
BW41	SM	WR	SM-Group 1	67.9	0.54	16.3	3.37	0.06	1.14	3.26	4.02	3.38	-		-
BW32	SM	WR	SM-Group 1	64.6	0.50	18.8	2.22	0.05	0.44	1.53	4.76	7.16	-		-
SWZ	SM	WR	SM-Group 1	63.6	0.87	17.8	3.71	0.09	1.36	2.75	4.74	5.10	-		-
SML213	SM	WR	SM-Group 1	63.9	1.00	16.3	4.84	0.09	1.87	3.82	3.88	4.27	-		-
BGZ	SM	WR	SM-Group 2	74.0	0.23	14.3	1.41	0.00	0.34	1.48	3.64	4.63	-		-
BW11	SM	WR	SM-Group 2	72.4	0.34	14.4	2.16	0.00	0.80	2.11	3.79	3.98	-		-
BW63	SM	WR	SM-Group 2	73.2	0.23	14.3	1.72	0.00	0.51	1.65	3.49	4.89		449	Q2F
BD3	SM	WR	SM-Group 2	72.9	0.27	14.6	1.82	0.00	0.63	1.79	3.50	4.53	-		-
BD9	SM	WR	SM-Group 2	72.7	0.33	14.4	1.87	0.00	0.53	1.69	3.66	4.81	-		-
BD18	SM	WR	SM-Group 2	73.4	0.27	14.3	1.72	0.00	0.52	1.56	3.49	4.69		433	Q2F
BD35	SM	WR	SM-Group 2	73.3	0.27	14.2	1.74	0.00	0.48	1.60	3.58	4.74		442	Q2F
BD39	SM	WR	SM-Group 2	72.7	0.30	14.5	1.90	0.00	0.59	2.07	3.58	4.40		423	Q2F
MI-1	SM	WR	SM-Group 2	74.0	0.32	13.7	1.98	0.00	0.62	1.86	3.29	4.27	-		-
SML120Z	SM	WR	SM-Group 2	74.1	0.25	13.8	1.59	0.00	0.42	1.19	3.35	5.30	-		-
MI-2	SM	WR	SM-Group 2	74.2	0.27	13.8	1.79	0.00	0.56	1.59	3.32	4.39	-		-
BW40	SM	WR	SM-Group 2	74.4	0.23	13.8	1.44	0.05	0.36	1.22	3.83	4.67		377	Q2F
BW36	SM	WR	SM-Group 2	73.7	0.23	14.3	1.21	0.04	0.32	1.11	3.91	5.15	-		-
BW43	SM	WR	SM-Group 2	75.0	0.25	13.4	1.55	0.05	0.51	1.40	3.83	3.98	-		-
BCOZ	SM	WR	SM-Group 2	72.5	0.29	14.7	1.86	0.04	0.50	1.63	3.67	4.80	-		-
MPL53Z	SM	WR	SM-Group 2	74.0	0.24	13.9	1.68	0.00	0.54	1.56	3.40	4.73		399	Q2F
BW47	SM	WR	SM-Group 3a	77.1	0.06	13.3	0.47	0.00	0.04	0.72	4.32	4.03	-		-
LGZ	SM	WR	SM-Group 3a	76.9	0.13	12.7	0.83	0.00	0.10	0.67	3.92	4.76		220	Q2FMI
BW48	SM	WR	SM-Group 3a	75.7	0.23	13.1	1.22	0.05	0.29	0.93	3.98	4.47		294	Q2F
SML52	SM	WR	SM-Group 3a	77.1	0.16	12.5	0.89	0.00	0.13	0.48	4.05	4.63		187	Q2FMI
SML49Z	SM	WR	SM-Group 3b	77.5	0.12	12.5	0.61	0.00	0.09	0.43	4.08	4.70		177	Q2FMI
SML47	SM	WR	SM-Group 3b	77.4	0.14	12.3	0.76	0.00	0.13	0.56	3.44	5.23		132	Q2FMI
SML63C	SM	WR	SM-Group 3b	77.4	0.21	12.1	1.31	0.00	0.11	0.24	3.63	5.06	-		-

SML67	SM	WR	SM-Group 3b	78.6	0.10	12.1	0.60	0.00	0.04	0.38	3.95	4.23	-		-
SML69	SM	WR	SM-Group 3b	78.0	0.09	12.2	0.52	0.00	0.07	0.43	3.95	4.68		130	Q2FMI
SML71	SM	WR	SM-Group 3b	78.2	0.13	11.9	0.73	0.00	0.07	0.40	3.91	4.58	-		-
SML73	SM	WR	SM-Group 3b	78.0	0.12	12.1	0.69	0.00	0.07	0.33	3.87	4.80	-		-
SML74	SM	WR	SM-Group 3b	77.7	0.12	12.3	0.66	0.00	0.07	0.40	3.95	4.81		151	Q2FMI
SML76	SM	WR	SM-Group 3b	77.6	0.07	12.4	0.66	0.00	0.05	0.35	4.31	4.50		171	Q2FMI
SML78	SM	WR	SM-Group 3b	78.7	0.08	12.0	0.54	0.00	0.03	0.20	4.19	4.26	-		-
SML129Z	SM	WR	SM-Group 3b	78.0	0.12	12.1	0.69	0.00	0.07	0.33	3.87	4.80	-		-
SML130	SM	WR	SM-Group 3b	77.7	0.12	12.3	0.66	0.00	0.07	0.40	3.95	4.81		151	Q2FMI
SML132	SM	WR	SM-Group 3b	77.6	0.07	12.4	0.66	0.00	0.05	0.35	4.31	4.50		171	Q2FMI
SML133	SM	WR	SM-Group 3b	78.7	0.08	12.0	0.54	0.00	0.03	0.20	4.19	4.26	-		-